Newcastle University

ePrints

Rismondo J, Cleverley RM, Lane HV, Grosshennig S, Steglich A, Moller L, Mannala GK, Hain T, Lewis RJ, Halbedel S. Structure of the bacterial cell division determinant GpsB and its interaction with penicillin-binding proteins. ***Molecular Microbiology***

Copyright:

This is the peer reviewed version of the following article: Rismondo J, Cleverley RM, Lane HV, Grosshennig S, Steglich A, Moller L, Mannala GK, Hain T, Lewis RJ, Halbedel S. Structure of the bacterial cell division determinant GpsB and its interaction with penicillin-binding proteins. *Molecular Microbiology* 2015, which has been published in final form at http://dx.doi.org/10.1111/mmi.13279 This article may be used for non-commercial purposes in accordance with Wiley Terms and Conditions for Self-Archiving.

Date deposited:

09/12/2015

Embargo release date:

17 November 2016

This work is licensed under a
Creative Commons Attribution-NonCommercial-NoDerivatives 4.0 International licence

Newcastle University ePrints - eprint.ncl.ac.uk

molecular microbiology

Structure of the bacterial cell division determinant GpsB and its interaction with penicillin binding proteins

Journal:	*Molecular Microbiology*
Manuscript ID	MMI-2015-15485.R1
Manuscript Type:	Research Article
Date Submitted by the Author:	n/a
Complete List of Authors:	Rismondo, Jeanine; Robert Koch Institute, FG11 Division of Enteropathogenic bacteria and Legionella Cleverley, Robert; Newcastle University, Institute for Cell and Molecular Biosciences Lane, Harriet; Newcastle University, Institute for Cell and Molecular Biosciences Großhennig, Stephanie; Universität Göttingen, Abteilung Allgemeine Mikrobiologie; Robert Koch Institute, FG11 Division of Enteropathogenic bacteria and Legionella Steglich, Anne; Robert Koch Institute, FG11 Division of Enteropathogenic bacteria and Legionella Möller, Lars; Robert Koch Institute, ZBS 4 - Advanced Light and Electron Microscopy Mannala, Gopala; University of Gießen, Institute of Medical Microbiology Hain, Torsten; Justus-Liebig University School of Medicine, Institute of Medical Microbiology Lewis, Richard; University of Newcastle, Institute for Cell and Molecular Biosciences Halbedel, Sven; Robert Koch Institute, FG11 Division of Enteropathogenic bacteria and Legionella
Key Words:	peptidoglycan, pathogenicity, cytokinesis, membrane binding, DivIVA

SCHOLARONE™
Manuscripts

Structure of the bacterial cell division determinant GpsB and its interaction with penicillin binding proteins

Jeanine Rismondo[1], Robert M. Cleverley[2], Harriet V. Lane[2], Stephanie Großhennig[1,3], Anne Steglich[1], Lars Möller[4], Gopala Krishna Mannala[5], Torsten Hain[5], Richard J. Lewis[2], and Sven Halbedel[1,*]

[1] FG11 Division of Enteropathogenic bacteria and *Legionella*, Robert Koch Institute, Wernigerode, Germany

[2] Institute for Cell and Molecular Biosciences, University of Newcastle, Newcastle upon Tyne, United Kingdom

[3] Department of General Microbiology, Institute of Microbiology and Genetics, Georg-August University, Göttingen, Germany

[4] ZBS 4 - Advanced Light and Electron Microscopy, Robert Koch Institute, Berlin, Germany;

[5] Institute of Medical Microbiology, University of Gießen, Gießen, Germany

[*] Corresponding author:

E-Mail: halbedels@rki.de, address: Robert Koch Institute, FG11 Division of Enteropathogenic bacteria and *Legionella*, Burgstrasse 37, D-38855 Wernigerode, Germany; phone: +49-30-18754-4323; fax: +49-30-18754-4207;

Short title: *Listeria monocytogenes GpsB*

Keywords: peptidoglycan/ pathogenicity/ cytokinesis/ membrane binding/ DivIVA

For Peer Review

Summary

Each bacterium has to co-ordinate its growth with division to ensure genetic stability of the population. Consequently, cell division and growth are tightly-regulated phenomena, albeit different bacteria utilise one of several alternative regulatory mechanisms to maintain control. Here we consider GpsB, which is linked to cell growth and division in Gram-positive bacteria. Δ*gpsB* mutants of the human pathogen *Listeria monocytogenes* show severe lysis, division and growth defects due to distortions of cell wall biosynthesis. Consistent with this premise, GpsB interacts both *in vitro* and *in vivo* with the major bi-functional penicillin binding protein. We solved the crystal structure of GpsB and the interaction interfaces in both proteins are identified and validated. The inactivation of *gpsB* results in strongly attenuated virulence in animal experiments, comparable in degree to classical listerial virulence factor mutants. Therefore, GpsB is essential for *in vitro* and *in vivo* growth of a highly virulent food-borne pathogen, suggesting that GpsB could be a target for the future design of novel antibacterials.

For Peer Review

Introduction

Bacteria require a multitude of regulatory factors to co-ordinate cycles of growth and division to ensure genetic stability of the population. Despite the essentiality of the co-ordination process, different bacteria have evolved a variety of regulatory mechanisms and factors. Whilst the universal tubulin homolog, FtsZ, forms the Z-ring that is required to drive the constriction of the cell division septum (Adams & Errington, 2009), the proteins that regulate FtsZ localization and dynamics are not conserved. For instance, the Z-ring is anchored to the membrane in *Escherichia coli* (a proteobacterium) by FtsA and ZipA (Hale & de Boer, 1997, Pichoff & Lutkenhaus, 2005), whereas in *Bacillus subtilis* (a firmicute), FtsA and the unrelated SepF fulfil this role (Duman *et al.*, 2013). In *Streptomyces* (from the phylum actinobacteria), FtsA is absent yet there are three orthologs of SepF, and mycobacteria have no FtsA and only one copy of SepF (Gola *et al.*, 2015). Similarly, the modulators of FtsZ in *B. subtilis* include EzrA and ZapA, in *E. coli* there is ZapA and ZapB, but there are no homologous gene products in *Streptomyces* (Adams & Errington, 2009, Jakimowicz & van Wezel, 2012). Consequently, it is important that the cell cycle of relevant bacteria – model organisms, significant pathogens – is better characterized so as to understand the major principles as well as for the development of novel antibiotics.

Amongst the other regulators of viability, cell growth and division in various Gram-positive bacteria is the DivIVA superfamily (Kaval & Halbedel, 2012, Lin & Thanbichler, 2013), which includes the DivIVA archetypes and the GpsB proteins (Massidda *et al.*, 1998, Claessen *et al.*, 2008, Tavares *et al.*, 2008, Land *et al.*, 2013, Fleurie *et al.*, 2014). Deletion of *B. subtilis gpsB* is without phenotype under normal conditions, however, Δ*gpsB* cells lyse and form polar bulges in high salt containing media. Bulging is a result of aberrant cell wall biosynthesis at the cell poles because of the delocalization of the major bi-functional penicillin binding protein 1 (PBP1). Bulging can also be observed under standard growth

For Peer Review

conditions when Δ*gpsB* is combined with a deletion in *ezrA*, a negative regulator of Z-ring formation (Claessen *et al.*, 2008). In *B. subtilis* PBP1 interacts directly with GpsB and EzrA (Claessen *et al.*, 2008), and these interactions determine the localization of PBP1 by an unknown mechanism. In *Streptococcus pneumoniae*, depletion of GpsB prevents closure of the divisome in a manner that is independent of PBP1 (Land *et al.*, 2013).

Unlike DivIVA (Lenarcic *et al.*, 2009, Ramamurthi & Losick, 2009), GpsB does not accumulate at curved membranes. Instead, it shuttles dynamically between the lateral sides of the cell cylinder, to which it localizes in elongating cells of *B. subtilis,* and the division septum upon the formation of the divisional Z-ring (Claessen *et al.*, 2008, Tavares *et al.*, 2008). Accumulation of *B. subtilis* GpsB at the septal ring occurs simultaneously with DivIVA and depends on late-acting division proteins, including DivIC and PBP 2B (Tavares *et al.*, 2008, Gamba *et al.*, 2009), but it is not yet known how GpsB is recruited to the septum and then back to the side wall of the cell. GpsB and DivIVA proteins share a highly conserved N-terminal domain, which in DivIVA is required for binding to curved membranes (Lenarcic *et al.*, 2009, Oliva *et al.*, 2010), as well as for interacting with membrane-bound cell division proteins (van Baarle *et al.*, 2013). By contrast, the C-terminal domains of GpsB and DivIVA are distinct, and this domain is used in DivIVA to interact with soluble cytosolic proteins (Donovan *et al.*, 2012, van Baarle *et al.*, 2013). The crystal structure of the N-terminal domain of DivIVA is a dimeric coiled-coil and solvent-exposed hydrophobic amino acid side chains are believed to insert into the membrane (Oliva *et al.*, 2010); the DivIVA C-terminal domain forms a long anti-parallel coiled-coil such that the full-length DivIVA is an extended tetramer (Oliva *et al.*, 2010). By contrast, the structure and function of the two domains of GpsB are unknown.

Here we investigate the role of GpsB in the physiology of *Listeria monocytogenes*, a human pathogen that causes serious food-borne infections with a mortality rate of 10-30% (Swaminathan & Gerner-Smidt, 2007). We show that GpsB is indispensable for growth and

For Peer Review

cellular integrity under standard laboratory conditions, leading to a strong attenuation of the Δ*gpsB* mutant in several infection models. We identify PBP A1 as the functionally relevant interaction partner of GpsB and demonstrate that this interaction is essential for functional PBP A1 activity. We also solve the crystal structures of both the N-terminal and C-terminal domains of GpsB, and confirm that a conserved, contiguous surface patch is used as the predominant PBP A1 binding site in the former. Together, these data confirm the key role of GpsB in growth and virulence, and highlight that cell division regulators could be useful new targets for the design of novel antibiotics.

For Peer Review

Results

L. monocytogenes GpsB

The *L. monocytogenes* EGD-e *lmo1888* gene product shares 56.7% sequence identity with *B. subtilis* GpsB (*Bs*GpsB) and is thus re-named *Lm*GpsB. *Lm*GpsB contains the highly conserved N-terminal domain (residues 1-69) typical of DivIVA/GpsB proteins (Fig. 1A). The *Lm*GpsB C-terminal region (residues 90-113) is significantly shorter than the coiled-coil C-terminal domain of DivIVA, but is also predicted to contain an amphipathic helix (Fig. S1A-B). The linker region (residues 70-89) is less well conserved than either terminus and is specific to the GpsB family.

*Lm*GpsB strongly self-interacted in a set of bacterial two-hybrid experiments (Fig. 1B). The self-interaction was retained when the C-terminal region was removed (GpsBΔC, residues 1-67), but the self-interaction was weakened somewhat when the N-terminal region was deleted (GpsBΔN, residues 68-113, Fig. 1C). These data indicate that both domains contribute to the self-interaction of GpsB. In fact, full-length GpsB proteins are hexamers in solution as determined by size exclusion chromatography - multi-angle laser light scattering (SEC-MALLS) (Fig. 1D), and equivalent N-terminal fragments – *Bs*GpsB$_{1-68}$ and *Lm*GpsB$_{1-73}$ – both form dimers (Fig. 1E). By contrast, the C-terminal domain of *Bs*GpsB (*Bs*GpsB$_{69-98}$) forms a trimer (Fig. 1F), suggesting that the GpsB hexamers consist of a trimer of dimers.

GpsB localization in *L. monocytogenes*

When GpsB-GFP was expressed in *L. monocytogenes*, the resultant fluorescence signal obeyed a bimodal distribution: cells either displayed bright septa with weaker peripheral fluorescence, or they only had peripheral fluorescence (Fig. 2A). 36% of all cells showed septal GpsB-GFP localization (76/212 cells), whereas 64% had not accumulated GpsB-GFP signals at the division septa (136/212 cells). Additional fluorescent foci were occasionally

For Peer Review

observed at one cell pole. Cells without the septal GpsB-GFP signal were significantly shorter (1.48±0.31 µm) than cells with septal GpsB-GFP (2.11±0.36 µm, $P<0.0001$, Fig. 2B) and GpsB-GFP stability was confirmed by Western blotting (Fig. 2C). These observations are in good agreement with a previous report that *B. subtilis* GpsB re-localized from the lateral sides of the cell cylinder in young, shorter, growing cells to the division septum as soon as longer, fully-grown cells started to divide (Claessen *et al.*, 2008). Western blots of cellular and membrane fractions of *L. monocytogenes* revealed that GpsB was enriched in membrane fractions (Fig. 2D), and membrane association was dependent on residues L24 and R25 (Fig. 2E). This cellular distribution mirrors that of DivIVA (Fig. 2D), which depends on the equivalent amino acids, F17 and R18 (Oliva *et al.*, 2010).

Effects of *gpsB* deletion on growth of *L. monocytogenes*

The Δ*gpsB* mutant (strain LMJR19) did not reveal a growth defect in BHI broth at 30 °C (Fig. 3A) but at 37°C it grew with reduced growth rate and only reached half of the final optical density of the wild type strain (Fig. 3B). Moreover, not all of Δ*gpsB* mutant cells are viable, as indicated by CFU-based growth measurements (Fig. S2A). This growth defect was rescued upon expression of GpsB-GFP (Fig. S2B). At 42 °C, however, the Δ*gpsB* strain showed a pronounced temperature-sensitive phenotype and did not grow at all (Fig. 3C). Western blotting confirmed the absence of GpsB in strain LMJR19 (Δ*gpsB*) and IPTG-dependent GpsB expression in the inducible mutant strain LMS56 (Fig. 3B), demonstrating that GpsB is important for growth during standard laboratory conditions and becomes essential at elevated temperatures.

Increased autolysis of *L. monocytogenes gpsB* mutant strains

Phase contrast microscopy revealed that the Δ*gpsB* mutant produced cells with bent shapes and many phase-bright cells (arrows in Fig. 4A), which represent lysed, dead cells; the Δ*gpsB*

For Peer Review

mutant suffers from increased autolysis. Scanning electron microscopy showed that the Δ*gpsB* mutant generated partially bent, slightly swollen and elongated cell types with the tendency to aggregate (Fig. 4B, Fig. S3). However, neither septum morphology nor cell wall thickness was affected in the Δ*gpsB* strain as determined by transmission electron microscopy of ultra-thin sections (Fig. S4). By contrast, the Δ*gpsB* mutant and the inducible *gpsB* mutant strain LMS56 had increased penicillin sensitivities in comparison to the wild type in the absence of IPTG (Fig. 4C). Penicillin exposure did not simply inhibit growth of the Δ*gpsB* strains, but actually induced bacteriolysis in quantitative autolysis experiments (Fig. 4D). Here penicillin was used to block peptidoglycan biosynthesis so that endogenous autolysis could be measured. Even in the absence of penicillin, the Δ*gpsB* mutant is more prone to lysis than the wild type, and addition of penicillin increased this effect about two-fold. By contrast, penicillin did not induce bacteriolysis of wild type cells at all (Fig. S5). These observations indicate that the cell wall is somehow weakened in the Δ*gpsB* mutant, and consistent with this, a two-fold increase in sensitivity against the cell wall hydrolase mutanolysin was observed for Δ*gpsB* cells (Fig. 4E).

Synthetic division defect of a *gpsB divIVA* double mutant

The similarity in sequence of their N-terminal domains, and their potential for functional redundancy, led us to construct a Δ*gpsB* Δ*divIVA* double mutant (strain LMJR28) to test whether this combination would result in a stronger phenotype than for either single deletion. A slight increase in cell lengths of the Δ*gpsB* and Δ*divIVA* single mutants in comparison to the wild type was observed (Table S1), however, average cell length was increased more than two-fold in the Δ*gpsB* Δ*divIVA* strain in comparison to the wild type (Fig. 5A-B, Table S1). Cell lengths of the Δ*gpsB* Δ*divIVA* double mutant showed a pronounced heterogeneity and reached values close to 10 µm (Fig. 5B). The cell width of the Δ*gpsB* Δ*divIVA* double mutant was the thinnest, whereas the width of both single mutants was close to wild type (Table S1).

For Peer Review

The synergism of the Δ*divIVA* and Δ*gpsB* phenotypes therefore suggests that these proteins have redundant and partially overlapping cell division functions.

GpsB controls PBP A1 and is essential for functional PBP A1 activity

GpsB is associated with the regulation of PBP1 in *B. subtilis* (Claessen *et al.*, 2008). In order to test which high molecular weight (HMW) PBP is affected in the absence of GpsB, all five *L. monocytogenes* HMW PBPs (Rismondo *et al.*, 2015) were introduced as a second IPTG-inducible copy in the Δ*gpsB* mutant. When the resulting strains were grown on BHI+IPTG plates, overexpression of *Lm*PBP A1 specifically impaired the growth of the Δ*gpsB* strain (Fig. 6A). This effect was confirmed in liquid culture and was not observed when *Lm*PBP A1 was overexpressed in wild-type cells (Fig. 6B). IPTG-dependent overexpression of *Lm*PBP A1 in both backgrounds was confirmed by SDS-PAGE and subsequent PBP staining using bocillin-fl (Fig. 6C), but did not cause any additional morphological aberrations in the Δ*gpsB* mutant strain LMJR33 (data not shown). Thus, growth of the Δ*gpsB* mutant is specifically sensitive to increased *Lm*PBP A1 levels, perhaps because *Lm*GpsB acts as a negative regulator of *Lm*PBP A1 activity.

If *Lm*PBP A1 activity is disregulated in the Δ*gpsB* mutant, then deletion of *pbpA1* should rescue the Δ*gpsB* phenotype. In fact, a Δ*gpsB* Δ*pbpA1* double mutant (LMJR38) could grow at 42 °C, in contrast to the Δ*gpsB* strain (Fig. 6D). However, the suppression of the Δ*gpsB* growth defect was not complete (Fig. 6D), indicating that other factors contributed to the Δ*gpsB* phenotype. Deletion of *pbpA1* in the Δ*gpsB* Δ*divIVA* double mutant background also corrected the cell division defect of this strain back to the level of the Δ*gpsB* single mutant (Fig. 6E), therefore, the Δ*gpsB* Δ*divIVA* division defect is mediated through *Lm*PBP A1. We could not find any differences in GFP-*Lm*PBP A1 localization patterns between wild type and a Δ*gpsB* strain (Fig. S6A). In both strains, GFP-*Lm*PBP A1 was present in bright bands at midcell and caused fainter signals at the cell periphery. Fluorescent vancomycin

For Peer Review

staining did not reveal significant differences between wild type and the Δ*gpsB* mutant (Fig. S6B) and *Lm*PBP A1 expression levels were similar in both strains (Fig. 6C). Taken together, these data suggest that *Lm*GpsB neither affects localization nor synthesis of *Lm*PBP A1.

Simultaneous inactivation of the two bi-functional PBPs, *Lm*PBP A1 and *Lm*PBP A2, is not tolerated by *L. monocytogenes* (Rismondo *et al.*, 2015), providing a means to determine if *Lm*GpsB is required for *Lm*PBP A1 activity. Despite repeated attempts, we were unable to generate a Δ*gpsB* mutant that also lacked *pbpA2*, indicating synthetic lethality of both genes. Therefore, a *gpsB* depletion strain was constructed that also contained a deletion in *pbpA2* (strain LMJR108). LMJR108 cells pre-depleted for *Lm*GpsB could grow in the presence of IPTG, but growth was strongly retarded in the absence of the inducer (Fig. 6F). Apparently, *Lm*PBP A2 becomes essential in the absence of *Lm*GpsB, suggesting that *Lm*PBP A1 is non-functional in the Δ*gpsB* mutant. We assume that the negative impact of GpsB on PBP A1, which we have postulated above, is a prerequisite for correct PBP A1 function.

The interaction of GpsB with PBP A1

Full-length *Lm*GpsB interacted strongly with full-length *Lm*PBP A1 in a bacterial two-hybrid experiment (Fig. 7A). Removal of the C-terminal domain of *Lm*GpsB did not impair *Lm*PBP A1 binding, whereas removal of the N-terminal domain, or introducing a mutation preventing dimerization of the N-terminal domain (V32A), abrogated binding completely. By contrast, L24A and R25A mutations had no effect (Fig. 7A).

We then used surface plasmon resonance (SPR) to probe the interaction between *Bs*GpsB in solution and *Bs*PBP1 (the orthologue of *Lm*PBP A1) that had been immobilised to the SPR chip surface. Full-length *Bs*GpsB bound with rapid kinetics to full-length *Bs*PBP1 and the binding data could be fitted to a 1:1 model with a K_d of 0.7±0.1 μM (Fig. 7B). By contrast, no binding of $BsGpsB_{69-98}$ to the chip surface was seen even when the injected protein was at a concentration of 200 μM (Fig. 7C). A K_d of 30±4 μM was obtained for the

For Peer Review

binding of *Bs*GpsB$_{1-68}$ to immobilised full-length *Bs*PBP1 (Fig. 7D). The >40-fold weaker binding of *Bs*GpsB$_{1-68}$ to *Bs*PBP1 might be a function of the different oligomerisation properties of *Bs*GpsB proteins: full-length, hexameric *Bs*GpsB has the capacity to interact with up to six *Bs*PBP1 molecules on an SPR chip, whereas the truncated N-terminal domain of *Bs*GpsB can only bind to two. Finally, a construct that lacked the entire cytoplasmic domain of *Bs*PBP1 (*Bs*PBP1$_{32-914}$) was immobilized onto an SPR chip surface. Demonstrable binding of *Bs*GpsB to the truncated *Bs*PBP1 protein was not observed (Fig. 7E). The removal of the cytoplasmic domain (amino acids 1-31) from *Lm*PBP A1 also caused a Δ*pbpA1*-like elongated phenotype in *L. monocytogenes* (Fig. S7A-B), confirming that the interaction of *Lm*PBP A1 with *Lm*GpsB is critical for *Lm*PBP A1 function. These observations – using different experimental procedures and proteins of different species – demonstrate conclusively that the interaction between GspB and the major bi-functional HMW PBP is limited to the small cytosolic N-terminal domain of the PBP.

Crystal structure of the N-terminal domain of GpsB

In order to understand the molecular basis of the GpsB:PBP interaction, the crystal structure of *Lm*GpsB$_{1-73}$ was solved (Fig. 8A, Table S2). Consistent with the SEC-MALLS data, *Lm*GpsB$_{1-73}$ in the crystals is a dimer formed by two identical subunits, each of which contains two α-helices spanning residues G12 to E17 and P29 to N66. The helices assemble into a four-helical bundle, the core of which buries hydrophobic amino acids from helices 1 (I15) and 2 (V32, F35, L36, V39, I40, Y43), and L10 from the coil immediately preceding helix 1 (Fig. 8A). A mutation in the hydrophobic core (V32A) caused almost complete loss of self-interaction in a two-hybrid analysis (Fig. 1C). Further hydrophobic amino acids of a near-perfect heptad sequence of a coiled-coil - F46, I50, L53, L60 and L64 - complete a buried hydrophobic stripe (Fig. 8A). The GSH tripeptide remnant of the thrombin-cleaved His$_6$-tag and the first nine *Lm*GpsB residues splay away from the main body of the protein and few

For Peer Review

contacts are made between the main body of the protein and the first nine residues (Fig. 8A). The ordering of this part of structure, despite the paucity of contacts to the main body of the protein, is explained by the crystal lattice (Fig. S8A).

The structure of *Bs*GpsB$_{1-68}$ was subsequently also solved (Fig. 8B, Table S2). The two *Bs*GpsB$_{1-68}$ dimers in the crystallographic asymmetric unit are essentially identical to each other, with monomer:monomer rmsds of 0.65±0.05 Å, which are comparable to the rmsds between *Bs*GpsB$_{1-68}$ and *Lm*GpsB$_{1-73}$ monomers of 0.64 ± 0.14 Å. The largest variations in structure between the orthologues are found in the flexible N-terminal regions (Fig. 8B), which participate in crystal contacts in both structures (Fig. S8A-C).

Given that the structure of DivIVA$_{1-65}$ was used to solve the structure of *Lm*GpsB$_{1-73}$, it is not surprising that the structures are highly similar: the rmsds in 48 matched Cα atoms between *Lm*GpsB$_{1-73}$ and DivIVA$_{1-65}$ monomers range between 0.50 and 1.12 Å, and the 96 matched Cα atoms in the dimers yields an rmsd of 0.96 Å. The two GpsB N-terminal domain structures reported here will serve as models for all members of the GpsB family, since the sequence insertions observed in some orthologues (Fig. 1A) are only of 3 and 4 amino acids in length, corresponding to single turns of an α-helix.

Crystal structure of the C-terminal domain of GpsB

The structure of *Bs*GpsB residues 76-98 (equivalent to *Lm*GpsB residues 89-111) was also solved by X-ray crystallography. Nine copies of the *Bs*GpsB$_{76-98}$ peptide are present in the asymmetric unit of the crystal lattice, which assemble into three stable trimers based on PDB-PISA (Krissinel & Henrick, 2007) analysis of the intermolecular interfaces. The three trimers superimpose on each other with rmsds of between 0.6 and 0.7 Å on matched Cαs. The trimer is a simple, triple-stranded parallel coiled-coil (Fig. 8C) that includes the highly conserved heptad repeat sequence between K82 and V91. The helical section encompasses residues F78

For Peer Review

to F92, and the peptides up- and down-stream, respectively, tends to lack regular secondary structure, show variation between chains, and in some chains are completely disordered.

There are over 300 PDB entries (representing ~90 non-redundant structures) that contain homotrimeric, parallel coiled-coils (Testa *et al.*, 2009), the majority of which are proteins that protrude from the surface of the 3-fold axes of the capsids of viruses and bacteriophages. The core helical region of the trimer can be superimposed on a representative three-stranded parallel coiled-coil (a mutant variant of the leucine-zipper GCN4, PDB code 1GCM (Harbury *et al.*, 1994)) with an rmsd of 1.5 Å on 51 matched Cαs, equivalent to 70% of the sequence of *Bs*GpsB$_{76\text{-}98}$ (Fig. S9A). A conserved RhxxhE sequence motif (h=hydrophobic residue) between residues R83 and E88 of *Bs*GpsB has been described previously in many three-stranded parallel coiled-coils (Kammerer *et al.*, 2005) and the characteristic features of this motif are retained in *Bs*GpsB$_{76\text{-}98}$ (Fig. 8D). First, within a *Bs*GpsB$_{76\text{-}98}$ trimer there are three bifurcated interhelical salt bridges between R83 and E88 residues; second, an ordered water molecule is observed between the sidechain Oε2 of E88 and the mainchain O of R83; third, the aliphatic portions of R83 and E88 pack against the buried hydrophobic residues (L84, L87 and V91) in the heptad repeat sequence; fourth, the leucines at positions 2 and 5 of the RhxxhE motif (L84 and L87) are the second-most and the most frequently observed hydrophobic amino acids at these locations in the motif, to optimise the packing between helices. These characteristics aid to stabilise the trimer.

None of the arrangements between the trimers in the crystal packing are calculated to be stable by PDB-PISA, consistent with the isolated domain being trimeric in solution (Fig. 1F). However, in the context of the hexameric full-length GpsB, the dimerization of the N-terminal domains probably provides an additional driving force promoting the association of the C-terminal domain trimers. The formation of the hexamer might therefore require the highly conserved hydrophobic amino acids F78, L81 and F92, which are solvent exposed in isolated trimers but are buried in the crystal lattice (Fig. S9B).

For Peer Review

Mutational analysis of structurally relevant GpsB residues

A notable feature of both structures of the N-terminal domain of GpsB is an elliptical-shaped surface cavity, some 7 Å wide, 12 Å long and 5 Å deep. In *Lm*GpsB$_{1-73}$ the cavity is formed by a series of conserved, mostly negatively-charged amino acids including L16, E19, K21, T22, Y27, S28, E30, D31, D33, E34, L36, D37, and I40 (Fig. 8E-F). This structure could drive the interaction with the positively-charged amino acids in the cytoplasmic domain of the corresponding PBP. Bacterial two-hybrid revealed that *Lm*GpsB residues Y27, V32, D33, L36, D37 and I40 were essential for the interaction with PBP A1 (Fig. 8G). V32 and L36 were also critical for dimerization of the N-terminal domain (Fig. 1C and data not shown). Residues Y27, D33, D37 and I40 form a single, contiguous surface patch at the edge of the cavity (Fig. 8H), whereas the base of the cavity is formed predominantly by L36, which thus plays dual roles in stabilizing the dimer and in PBP A1 binding.

The effect of *gpsB* mutations affecting dimerization (V32A, L36A) and *Lm*PBP A1 binding (Y27A, D33A, D37A, I40A) was analyzed in a complementation assay testing restoration of growth of the Δ*gpsB* mutant at 42°C (Fig. 9A). All mutated *Lm*GpsB variants were expressed as shown by Western blotting (Fig. 9B). Mutations in the dimerization interface (V32A, L36A) were inactive (Fig. 9A). Alleles with mutations in the *Lm*PBP A1 binding site fell into two classes: D37A and I40A showed intermediate phenotypes, whereas D33A and Y27A were completely inactive (Fig. 9A). D37 and I40 are located on the upper part of the surface cleft, whereas Y27 and D33, and V32 and L36 are oriented towards the bottom or the base of the depression, respectively (Fig. 8H, 9C). Y27 and D33 were unaffected in self-interaction in bacterial two-hybrid whereas V32 and L36 impaired GpsB self-interaction (Fig. 1C and data not shown).

SPR of the *Bs*GpsB$_{1-68}$D31A/D35A (corresponding to D33A and D37A in *Lm*GpsB) double mutants against immobilized *Bs*PBP1 both yielded K_ds more than 4-fold higher than that of the wildtype interaction (Fig. 7D). Furthermore, the D31A/D35A mutation completely

For Peer Review

abrogated binding of *Bs*GpsB$_{1-68}$ to a peptide encompassing the cytoplasmic domain of *Bs*PBP1. *Bs*GpsB$_{1-68}$ bound to a fluorescein-labelled *Bs*PBP1$_{1-32}$ (*Bs*PBP1 residues 1-32) peptide with a dissociation constant of 90±10 µM, measured by fluorescence polarization. By contrast, the *Bs*GpsB$_{1-68}$ D31A/D35A mutant did not bind the same peptide even at 500 µM protein concentration (Fig. 7F). By circular dichroism the D31A/D35A mutation had no discernible effect on the folding of *Bs*GpsB$_{1-68}$: thermal denaturation curves of the wild type and D31A/D35A *Bs*GpsB$_{1-68}$ proteins were identical (Fig. S10). The effect of the mutation on the GpsB:PBP interaction is thus not an indirect consequence of destabilizing the fold of the mutated GpsB proteins, but primarily due to the loss of specific contacts between the interacting partners. Furthermore, the details of the GpsB-PBP1 interaction identified here are perhaps mimicked by the crystal contacts in the structure of *Bs*GpsB$_{1-68}$, in which the His$_6$-tag remnant from one *Bs*GpsB$_{1-68}$ molecule interacts with residues in another *Bs*GpsB$_{1-68}$ molecule that are essential for the GpsB:PBP interaction (Fig. S8D).

Finally, the structure of *Bs*GpsB$_{76-98}$ revealed that residues R83 and E88, equivalent to R96 and E101 in *Lm*GpsB, are involved in a network of salt bridges between chains that stabilise the trimeric form of the C-terminal domain (Fig. 8D). Consistent with this key structural role, R96A and E101A *gpsB* mutant alleles were unable to complement the growth defect of the Δ*gpsB* mutant at 42°C (Fig. 9D-E). Purified Strep-tagged versions of the R96A and E101A GpsB proteins also ran aberrantly on blue native PAGE gels (Fig. 9F). R96A and E101A are thus critical for the formation of GpsB hexamers, an absolute requirement for GpsB function.

Attenuation of the Δ*gpsB* mutant in various infection models

The impact of GpsB on the virulence of *L. monocytogenes* was tested in infection experiments using J774 mouse ascites macrophages at 37°C. This temperature is required for induction of virulence gene expression through the master regulator PrfA, whereas PrfA-dependent

For Peer Review

virulence genes are silent at 30°C (Johansson *et al.*, 2002). GpsB does not influence phagocytosis by macrophages (t=0 in Fig. 10A). However, intracellular multiplication of the Δ*gpsB* mutant lagged more than four-fold behind that of the wild type (t=6 in Fig. 10A). Cell-to-cell spread of the wild type and the Δ*gpsB* mutant were compared in a plaque formation assay using 3T3 mouse embryo fibroblasts. Monolayers of fibroblasts were infected and formation of plaques corresponding to zones of killed host cells was visualised on the third day post infection by counterstaining with neutral red. A marginal reduction of plaque size formed by Δ*gpsB* mutant cells was observed (Fig. 10B). Apparently, the inherent growth defect of the Δ*gpsB* mutant cannot be complemented by host cell factors and rather leads to reduced intracellular proliferation rates.

Further infection experiments were performed using larvae of the wax moth *Galleria mellonella* as host (Mukherjee *et al.*, 2010). Only 43.3±5.8% of the larvae infected with the wild type strain EGD-e were still viable seven days post infection, whereas 90±10% of the larvae infected with the Δ*gpsB* mutant survived the infection until the seventh day of the experiment (Fig. 10C). Remarkably, this degree of attenuation is similar to that of a mutant lacking the pathogenicity island LIPI-1, which encodes six of the major *L. monocytogenes* virulence factors *prfA*, *plcA*, *hly*, *mpl*, *actA*, and *plcB* and caused survival rates of ~90% in an identical experiment (Mukherjee *et al.*, 2010). Taken together, these results demonstrate that GpsB is required for full pathogenicity of *L. monocytogenes*.

For Peer Review

Discussion

GpsB and its relative, DivIVA, are essential for growth and cell division in diverse Gram-positive bacteria (Fadda *et al.*, 2003, Ramirez-Arcos *et al.*, 2005, Nguyen *et al.*, 2007, Letek *et al.*, 2008, Halbedel *et al.*, 2012, Land *et al.*, 2013). Here we show that GpsB contributes to growth of *L. monocytogenes* through an interaction with PBP A1 and that this has consequences for virulence of this important human pathogen.

The cellular localization of GpsB is dynamic and dependent on cell cycle progression. In *B. subtilis,* septal GpsB localization depends on early (FtsZ, FtsA) and late cell division proteins (PbpB, DivIC) (Tavares *et al.*, 2008). DivIVA, which assembles at the division site only after constriction has started (Eswaramoorthy *et al.*, 2011), is not required for the septal localization of GpsB (Tavares *et al.*, 2008, Fleurie *et al.*, 2014). Thus, the septal localization of GpsB depends only on those divisome components that are essential for Z-ring assembly and constriction. How GpsB is recruited to the septum is unknown. GpsB might interact with a component of the divisome, but also could be a second example of a curvature-sensitive membrane binding protein with the intrinsic capability to cluster at curved membrane regions.

That the *gpsB* phenotype can be suppressed by deletion of *pbpA1* suggests that *Lm*PBP A1 activity becomes uncontrolled in the absence of *Lm*GpsB, which may act as a negative regulator of the PBP. The genetic relationships identified here are reminiscent of the situation in *B. subtilis*, where deletion of *ponA* (encoding PBP1) rescues the lytic phenotype of a *gpsB ezrA* double mutant (Claessen *et al.*, 2008). Moreover, the second bi-functional PBP (*Lm*PBP A2) becomes essential in the Δ*gpsB* mutant. Because at least one of the two bi-functional PBPs (A1 or A2) is required for growth of *L. monocytogenes* (Rismondo *et al.*, 2015), this indicates that *Lm*GpsB is in fact required for proper *Lm*PBP A1 function. Since the localization pattern of *Lm*PBP A1 was *Lm*GpsB-independent, *Lm*GpsB is not a targeting determinant for *Lm*PBP A1.

For Peer Review

More likely, the role of *Lm*GpsB is to link *Lm*PBP A1 with other divisome components and/or to link together individual *Lm*PBP A1 molecules as an important prerequisite for efficient biosynthesis of peptidoglycan. The linking of individual *Lm*PBP A1 molecules could affect wall synthesis by spatially coordinating PG synthesis activities within the divisome. Tight coordination of PG strand synthesis by transglycosylases and strand-strand crosslinking by transpeptidases has been found to be essential in molecular dynamics simulations of cell wall synthesis; in the absence of such coordination the integrity of the network of PG strands in the elongating cell wall breaks down (Nguyen *et al.*, 2015). The linkage of two PBP A1 molecules by GpsB could facilitate spatial coordination of PG strand synthesis and PG crosslinking given that the bi-functional PBP A1 has both transpeptidase and transglycosylase activities. In addition, other HMW bi-functional PBPs are known to dimerise and dimerization is important for producing nascent PG *in vitro* with the same degree of peptide cross-linking as seen *in vivo* (Bertsche *et al.*, 2005). A function of GpsB could thus be to promote dimerization of its cognate PBP to stimulate the associated transpeptidase activity. Overall, the observed negative genetic effect that GpsB exerts on PBP A1 could be due, therefore, to GpsB mediating a spatial restriction of PBP A1 activity within the divisome. While this GpsB function may not be essential for viability, as long as the second bi-functional PBP (PBP A2) is present, it clearly becomes essential in its absence.

The sequestration of PBP A1 in complex with GpsB would be lost by deletion of either protein, or by mutation of critical interfacing residues. Indeed, in both *B. subtilis* and in *L. monocytogenes*, mutation of conserved residues of the negatively-charged surface pocket in the N-terminal domain of GpsB resulted in a *gpsB* null phenotype *in vivo* and reduced binding constants for the *Bs*GpsB:*Bs*PBP1 interaction *in vitro*. This binding motif is better conserved among GpsB orthologues than the equivalent residues in DivIVA proteins (Fig. S11), which implies that interaction partners of GpsB are conserved in the different organisms but are different from those of DivIVA. In fact GpsB interacts with PBPs whilst DivIVA is known to

For Peer Review

bind to the transmembrane protein MinJ (van Baarle *et al.*, 2013), and interactions between DivIVA and PBPs have not yet been reported. However, the combination of Δ*gpsB* and Δ*divIVA* alleles caused a synergistic deleterious effect on *L. monocytogenes* cell division. This suggests that both proteins are part of parallel pathways that share an overlapping function during cytokinesis, and that they may share a common (but still to be identified) interaction partner. Remarkably, a fundamentally different situation is observed in *S. pneumoniae*; in this organism, deletion of *divIVA* cured the cell division defect of a Δ*gpsB* mutant that led to helical FtsZ rings unable to undergo productive division events (Fleurie *et al.*, 2014). The reason for this diversity is not yet clear, but it could be the consequence of general differences in the interplay of cell growth and cell division between rod-shaped and coccoid bacteria.

GpsB must control processes beyond PBP A1-dependent peptidoglycan biosynthesis in *L. monocytogenes*, as indicated by the following genetic data: (i) Deletion of *pbpA1* only partially suppressed the Δ*gpsB* growth defect at 42°C. (ii) Growth of the Δ*pbpA1* mutant is only marginally impaired at 42°C (Rismondo *et al.*, 2015), while the Δ*gpsB* mutant cannot grow under this condition. (iii) Mutations in the PBP A1 binding site of GpsB cause a *gpsB* null phenotype, whereas deletion of the GpsB binding site in PBP A1 only causes an intermediate *pbpA1* phenotype. We thus conclude that GpsB binds other, yet to be identified, proteins using an interaction surface that overlaps at the very least with that for binding PBPs. Furthermore, *pbpA1* deletion completely cures the synergistic cell division defect of a Δ*gpsB* Δ*divIVA* double mutant, which in turn, suggests that PBP A1 is the main effector of GpsB function with regard to cell division. Hence, GpsB interaction partners other than PBP A1 might be rather relevant for growth at elevated temperatures.

The N-terminal domains of GpsB and DivIVA are highly homologous in structure (Fig. S8E) and share some common functionalities; the N-terminal domains in both proteins are also necessary for the interaction with the membrane, and equivalent residues in the

For Peer Review

domains play essential roles in this association. However, their C-terminal domains are distinct; DivIVA is an anti-parallel tetramer (Oliva *et al.*, 2010) formed by the close packing of a lengthy C-terminal coiled coil. By contrast, GpsB is hexameric and the C-terminal domain, although a coiled-coil, is a trimer, with a parallel alignment of helices. It follows that the building blocks of the hexamer are three N-terminal domain dimers and two C-terminal domain trimers. The hexamerisation of GpsB must be important for function *in vivo* as mutations to the R/E salt bridge that disrupt the trimerisation of the C-terminal domain have a *gpsB* null phenotype, an observation that is consistent with changes in oligomeric state (to n = 2, 4 and 8) when the R/E salt bridge is lost by mutation in other triple-stranded coiled-coils (Kammerer *et al.*, 2005). Perhaps the most logical arrangement of GpsB subunits, which maintains an equivalent distance between covalently linked N and C terminal domains on all subunits, is a tripod-like arrangement (Fig. S9C). In this arrangement the two C-terminal domain trimers form the base of the tripod and the three N-terminal domain trimers form the legs of the tripod. One such a model might assume a relatively straight path between the covalently linked N- and C-terminal domains. However, there is typically at least one proline in the interdomain linker of GpsB proteins, and the linkers sequences display regions of obvious low complexity (Fig. 1A), suggesting that the subunits' dynamic arrangement specifically requires a linker that can follow a bent path.

Finally, inactivation of GpsB induced autolysis in response to penicillin, whereas penicillin did not induce bacteriolysis of Δ*pbpA1* cells (Rismondo *et al.*, 2015). We have also demonstrated that GpsB is required for full pathogenicity of *L. monocytogenes* in animal models. Since β-lactam antibiotics generally act bacteriostatically on *L. monocytogenes* and do not induce bacteriolysis (Hof, 2004, Lemaire *et al.*, 2005, Grayo *et al.*, 2008), a combination of β-lactams and novel GpsB inhibitors could provide an efficient future therapy for the treatment of listeriosis.

For Peer Review

Experimental Procedures

Bacterial strains and growth conditions

All strains used in this study are listed in Table S3. *L. monocytogenes* was generally cultivated in BHI broth or on BHI agar plates at 37°C if not stated otherwise. Where required, antibiotics and supplements were added at the following concentrations: erythromycin (5 µg mL^{-1}), kanamycin (50 µg mL^{-1}), X-Gal (100 µg mL^{-1}) and IPTG (1 mM). *Escherichia coli* TOP10 was used as standard cloning host (Sambrook *et al.*, 1989).

General methods, manipulation of DNA and oligonucleotide primers

Transformation of *E. coli* and isolation of plasmid DNA was performed using standard methods (Sambrook *et al.*, 1989). Preparation of electro-competent *L. monocytogenes* cells and transformation of *L. monocytogenes* were carried out as described elsewhere (Monk *et al.*, 2008). Restriction and ligation of DNA was done as described by the manufacturer´s instructions. For restriction free modification of plasmids an altered version of the original QuikChange mutagenesis protocol was employed (Zheng *et al.*, 2004). All primer sequences are listed in Table S4. Penicillin G test strips (0.016-256 µg mL^{-1}, Bestbiondx, Germany) were used for penicillin sensitivity assays. *L. monocytogenes* strains were grown in BHI broth and used to swab-inoculate BHI agar plates. Penicillin test strips were placed on top of the agar surface and the plates were incubated at 37°C for one day.

Plasmid and strain construction, protein purification

Construction of plasmids and *L. monocytogenes* strains as well as all protocols for overproduction and purification of recombinant proteins can be found in the supplementary materials section.

For Peer Review

Crystallisation and structure determination of GpsB proteins

Initial crystallisation conditions for *Lm*GpsB$_{1-73}$, *Bs*GpsB$_{1-68}$ and *Bs*GpsB$_{76-98}$ were obtained at 20°C by sitting-drop vapour diffusion; 100 nl of protein and screen solutions were pipetted by a TTP Labtech Mosquito. An initial crystallisation hit was obtained with *Lm*GpsB$_{1-73}$ at a concentration of 30 mg mL^{-1} in a buffer of 2 mM Tris.HCl pH 8.0 10 mM NaCl versus condition D1 of the Morpheus screen (Molecular Dimensions), which contains a buffer of 0.1 M MES.NaOH, 0.1 M imidazole pH 6.5, 10% PEG 20K, 20% PEG 550 MME and 0.02 M mixture of alcohol additives. For *Lm*GpsB$_{1-73}$, the crystallisation conditions were optimised in 96-well MRC plates. After 1-2 weeks of growth, *Lm*GpsB$_{1-73}$ crystals were harvested and mounted in rayon fibre loops in the crystallization well solution and flash frozen directly in liquid nitrogen prior to data collection using beamline IO4 of the Diamond light source at 100K and a wavelength of 0.9795 Å. The diffraction data were indexed and integrated in XDS (Kabsch, 2010) and scaled in SCALA (Evans, 2006). The *Lm*GpsB$_{1-73}$ structure was solved by molecular replacement in PHENIX (McCoy *et al.*, 2007) using a search model prepared from the structure of the DivIVA lipid binding domain (PDBid 2WUJ (Oliva *et al.*, 2010)) with CHAINSAW (Stein, 2008). This procedure correctly positioned two protein monomers in the asymmetric unit, consistent with a Matthews' co-efficient of 2.08 Å^3 Da^{-1} and a solvent content of 40.8 %. The molecular replacement solution was subsequently refined with PHENIX-REFINE (Adams *et al.*, 2010) and missing N- and C-terminal regions of the model were built automatically using ARP-WARP (Langer *et al.*, 2008). Subsequent manual alterations to the atomic model were made in COOT (Emsley *et al.*, 2010), interspersed with rounds of refinement in PHENIX.REFINE (Adams *et al.*, 2010) until convergence was reached. In the Ramachandran plot of the final structure, 99.3% of residues are in the most favoured regions with no outliers.

For *Bs*GpsB$_{1-68}$, sitting-drop crystallization screens were set up at a protein concentration of 10 mg mL^{-1} at 20°C. Crystals from well E9 of the INDEX (Hampton) screen

For Peer Review

(buffer conditions 0.05 M Bis-Tris.HCl pH 6.5, 0.05 M ammonium sulphate, 30% pentaerythyritol ethoxylate), were harvested in rayon fibre loops and frozen directly in liquid nitrogen. Diffraction data collected from Diamond synchrotron beamline IO4 at 100K and a wavelength of 0.9795 Å were also integrated with XDS (Kabsch, 2010) and scaled with SCALA (Evans, 2006). A search model derived from the coordinates of *Lm*GpsB$_{1-73}$ using CHAINSAW (Stein, 2008) was used in molecular replacement in PHENIX (McCoy *et al.*, 2007), positioning two *Bs*GpsB$_{1-68}$ dimers in the asymmetric unit, consistent with a Matthews' coefficient of 2.31 Å^3 Da^{-1} and a solvent content of 46.7%. The missing N- and C-terminal regions of the model were automatically built onto the molecular replacement solution using BUCCANEER (Cowtan, 2006) and the model was manually rebuilt in COOT (Emsley *et al.*, 2010) and refined in PHENIX.REFINE (Adams *et al.*, 2010). In the Ramachandran plot of the final structure, 97.3% of residues are in the most favoured regions with no outliers.

*Bs*GpsB$_{76-98}$ was subjected to spare-matrix crystallization screening at a concentration of 10 mg mL^{-1} in 10 mM HEPES.NaOH pH 7.5, 100 mM NaCl buffer and crystallized in several conditions of the PACT screen (Molecular Dimensions); the most consistent quality crystals were obtained in condition E1, which contains 0.2 M NaF and 20% PEG 3350. After optimization of the precipitant concentration in 96 well MRC plates, the crystals were cryoprotected by step-wise transfer in rayon loops to a cryoprotectant solution containing 0.2 M NaF, 20% glycerol and 24% PEG 3350; the first step involved a transfer to a mixture of 50% well solution and 50% cryoprotectant for 10-30 seconds, followed by transfer to 100% cryoprotectant for another 10-30 s before mounting in a rayon loop and plunging into liquid nitrogen. Diffraction data were recorded at Diamond beamline IO3 at 100K and a wavelength of 0.61992 Å; to maximize the completeness of the data from these triclinic crystals, three 180° data sets were collected from the same crystal at different crystal to detector distances. The individual datasets were integrated and scaled with the XDS (Kabsch, 2010) INTEGRATE and CORRECT modules, before merging all three datasets with AIMLESS

For Peer Review

(Evans & Murshudov, 2013). An initial polyalanine model was derived from the diffraction data using the *ab initio* phasing software ARCIMBOLDO (Sammito *et al.*, 2013). The initial model was rebuilt in COOT (Emsley *et al.*, 2010) against the electron density map calculated from the preliminary model phases and the model was subsequently subjected to iterated cycles of refinement in PHENIX.REFINE (Adams *et al.*, 2010) and modification in COOT (Emsley *et al.*, 2010). The diffraction data used for model refinement were cut at a resolution of 1.2 Å; although the data signal to noise was still respectable at this resolution and the data completeness decreased rapidly at resolutions higher than 1.2 Å. In the Ramachandran plot of the final structure, 100% of residues are in the most favoured regions. Validation of all structures was performed in MolProbity (Chen *et al.*, 2010) and summaries of the data collection and model refinement statistics are provided in Table S2.

Surface plasmon resonance.

All SPR experiments used a Biacore X100 instrument. For the initial immobilization of *Bs*PBP1 proteins, the Biacore CM5 chip was equilibrated in a buffer of 10 mM HEPES.NaOH pH 7.5, 200 mM NaCl, 0.1% reduced Triton X-100 (immobilization buffer) at a temperature of 25°C. Carboxyl groups on both flow cells on the chip surface were activated for amine coupling by the manufacturer's standard protocols and then 10 mg mL^{-1} ampicillin in 0.1 M sodium acetate pH 4.6 was injected over both flow cells at a flow rate of 10 µL min^{-1} for 9 minutes, followed by an identical injection of 1 M ethanolamine pH 8.0. The temperature of the chip surface was then adjusted to 35°C and *Bs*PBP1 proteins were then immobilised onto flow cell 2 by several 50-120 s injections (flow rate 10 µL min^{-1}) of 150 nM PBP1 (protein samples were incubated at 37°C for 4 min prior to injection onto the SPR) until 1400 response units of PBP1 had been immobilized. Titrations of *Bs*GpsB over the *Bs*PBP1 surface were undertaken at 25°C in a buffer of 10 mM Tris.HCl pH 8.0, 250 mM NaCl, 0.1% reduced Triton X-100 at a flow rate of 30 µL min^{-1}. For all of the GpsB injections, the response signal

For Peer Review

on the reference, protein-free surface (coated only with ampicillin [flow cell 1]) was subtracted from the response signal on the PBP1-coated surface (flow cell 2). At the end of each injection of GpsB, the chip surfaces were regenerated by 15-20 s injection with 50 mM HEPES.NaOH pH 7.5, 1 M NaCl, 2% reduced Triton X-100. For the interaction of both full length *Bs*GpsB and *Bs*GpsB$_{1-68}$ with immobilized *Bs*PBP1 the kinetics of binding were rapid, with binding reaching equilibrium within the timescale of an injection over a wide range of protein concentrations. The increase in response signal on the *Bs*PBP1 coated surface during an injection could therefore be used as a measure of equilibrium binding to *Bs*PBP1. The increase in response signal per injection was fitted versus injected protein concentration to a 1:1 model using the Biacore X-100 evaluation software. Each SPR titration was performed independently at least twice.

SEC-MALLS.

For *Bs*GpsB and *Bs*GpsB$_{1-68}$, 500 µL samples at concentrations of 1 mg mL^{-1} or 1.5 mg mL^{-1} were loaded onto Superdex200 or Superdex75 10/300 GL columns (GE Healthcare) respectively, equipped with a Jasco UV-2077 detector, Wyatt DAWN Heleos II EOS 18-angle laser photometer (with the 13th detector replaced with the QELS in-line dynamic light scattering detector) coupled to a Wyatt Optilab T-rEX refractive index detector. The flow rate was 0.75 ml min^{-1}.

For *Bs*GpsB$_{69-98}$, a 100 µL sample at 10 mg mL^{-1} concentration was loaded on a Superdex 200 Increase 10/300 GL column (GE Healthcare) on an Akta Pure operating at a flow rate of 0.5 mL min^{-1}, with column output fed into a DAWN Heleos II MALS detector with laser source at 664 nm and eight fixed angle detectors (Wyatt Technology, Santa Barbara, CA), followed by an Optilab T-rEX differential refractometer using 664 nm LED light source at 25°C (Wyatt Technology).

For Peer Review

The running buffer for all SEC-MALLS analyses was 10 mM Tris.HCl pH 8.0 250 mM NaCl. In all cases the molecular mass and concentrations of the peaks eluting from the column were analysed using Astra 6.2.

Circular dichroism

CD spectra were recorded on a JASCO J-810 spectropolarimeter interfaced to a PTC-423S Peltier temperature controller. GpsB proteins were at concentrations of 5 μM in a buffer of 25 mM sodium phosphate pH 7.3, 150 mM NaCl. CD data were collected using a 1 mm path length cuvette, at a wavelength of 222 nm, with a the response time of 8 s, a band width of 2 nm and the temperature was increased at a rate of 1°C per minute. To verify the reversibility of the temperature melts, full wavelength scans were recorded between 195 and 240 nm both before and after the melt; in all cases these CD spectra were superimposed on each other.

Fluorescence polarisation

Fluorescence polarisation was recorded in a PHERAstar FS (BMG Labtech) microplate reader using 386 well microplates. The excitation wavelength was 485 nm, and fluorescence emission was recorded above 520 nm. The focus and gain were adjusted based on a target polarization of 35 mP in wells containing free fluorescein-labelled peptide. Each data point corresponds to a 20 μL sample with 40 nM labelled peptide in 10 mM Tris.HCl pH 8.0, 250 mM NaCl. Binding data were fit to obtain a dissociation constant in Sigma Plot with the equation $P=P_{min}+P_{max}\{[protein]/(K_d+[protein])\}$ where P=polarisation, P_{min}=polarisation of free peptide, P_{max}=polarisation of peptide:protein complex, K_d = dissociation constant.

Blue native PAGE

NativePAGE Novex 4 to 16% Bis-Tris gels (Invitrogen) were used for separation of purified GpsB proteins by blue native PAGE. Gel runs were performed as specified by the instructions

For Peer Review

of the manufacturer. The NativeMark™ unstained protein standard (Novex) was used as a molecular weight marker.

Isolation of cellular proteins and Western blotting

Cells were harvested by centrifugation (13,000 rpm, 1 min in a table-top centrifuge) and washed once with ZAP buffer (10 mM Tris.HCl pH7.5, 200 mM NaCl). The cell pellet was resuspended in 1 mL ZAP buffer also containing 1 mM PMSF and disrupted by sonication. Cell debris was removed by centrifugation and the resulting supernatant was considered as total cellular protein extract. In order to separate membrane proteins from the soluble cytosolic proteins, the total cellular protein fraction was ultracentrifuged at 100,000 *g* for 30 min at 4°C. The supernatant contained the soluble cytoplasmic proteins and the pellet corresponded to the membrane fraction, which was resuspended in 100 µL ZAP buffer. Aliquots of these samples were separated by standard SDS polyacrylamide gel electrophoresis (12% acrylamide), whereas for separation of GpsB, 15% acrylamide gels were used. Gels were either stained using the colloidal coomassie agent Roti®-Blue (Roth, Germany) or transferred onto positively charged polyvinylidene fluoride (PVDF) membranes using a semi-dry transfer unit. Proteins of interest were immune-stained using polyclonal rabbit antisera recognizing DivIVA (Marston *et al.*, 1998), GFP (lab stock) or GpsB (this work) as the primary antibody and an anti-rabbit immunoglobulin G conjugated to horseradish peroxidase as the secondary one. The ECL chemiluminescence detection system (Thermo Scientific) was used for detection of the peroxidase conjugates on the PVDF membrane in a chemiluminescence imager (Vilber Lourmat).

PBP detection

In order to detect penicillin binding proteins in SDS-PAGE gels, aliquots corresponding to 20 µg of membrane proteins were incubated with 3 µM bocillin-fl (Molecular Probes) for 20 min

For Peer Review

at 37°C. The binding reaction was stopped by addition of loading dye and incubation for 5 min at 65°C. Samples were separated by SDS-PAGE using 8% polyacrylamide gels and PBPs were detected using a Fuji raytest FLA 2000 fluorescence scanner.

Bacterial two-hybrid analysis

GpsB self-interactions and interactions of GpsB with penicillin binding proteins were studied by the bacterial two-hybrid system (Karimova *et al.*, 1998). Plasmids encoding GpsB and PBPs fused to the T18 or the T25 fragment of the *Bordetella pertussis* adenylate cyclase were co-transformed in *E. coli* BTH101. Transformants were selected on nutrient agar plates containing ampicillin (100 µg mL^{-1}), kanamycin (50 µg mL^{-1}), X-Gal (0.004%), and IPTG (0.1 mM). The plates were photographed after 40 h of growth at 30°C.

Autolysis assays

L. monocytogenes strains were grown in BHI broth (containing 1 mM IPTG where required) at 37°C until an optical density of around OD_{600}=0.8 was reached. Cells were collected by centrifugation (6,000 *g*, 5 min, 4°C) and resuspended in 50 mM Tris.HCl pH8.0 to an optical density of OD_{600}=0.6. Penicillin (25 µg mL^{-1} final concentration) or mutanolysin (Sigma, 10 U mL^{-1}) was added and the cells were shaken at 37°C. Autolysis was followed by measuring the decrease in optical density (λ=600 nm) every 30 min in a spectrophotometer.

Microscopy

Samples (0.4 µL) were taken from exponentially growing bacterial cultures and transferred onto microscope slides which had been covered with a thin agarose film (1.5% in distilled water). The sample droplets were air-dried, covered with a cover lid and analysed by phase contrast or fluorescence microscopy. Membranes were stained by addition of 1 µL of Nile red solution (100 µg mL^{-1} in DMSO) to 100 µL of culture and shaking for 10 min at 37°C, before

For Peer Review

the cells were subjected to microscopy. Zones of nascent cell wall biosynthesis were visualized by addition of 3 µL vancomycin-fl (8 mM, Molecular Probes) to 100 µL of culture and shaking for 20 min at 37°C. Images were taken with a Nikon Eclipse Ti microscope coupled to a Nikon DS-MBWc CCD camera and processed using the NIS elements AR software package (Nikon) or ImageJ. Scanning electron microscopy and ultrathin section transmission electron microscopy were performed essentially as described earlier (Rismondo *et al.*, 2015).

Cell culture techniques

Intracellular growth in macrophages was analysed using J774.A1 mouse ascites macrophages (ATCC® TIB-67™) as described earlier (Halbedel *et al.*, 2014). Cell-to-cell spread was analysed in a plaque formation assay using 3T3 L1 mouse embryo fibroblast-like cells according to protocols published previously (Marquis, 2006, Halbedel *et al.*, 2012).

Insect infection model

Galleria mellonella larvae, purchased from fauna topics (Marbach, Germany), were reared at 32°C in darkness and on an artificial diet (22% maize meal, 22% wheat germ, 11% dry yeast, 17.5% bee wax, 11% honey and 11% glycerine) prior to use. Last instar larvae, each weighing between 250 and 350 mg, were used in all experiments as described previously (Mukherjee *et al.*, 2010). Fresh cultures of bacteria, prepared from an overnight culture, were used in all experiments. Bacteria were grown in BHI broth at 37°C, harvested during exponential growth and washed twice with 1×PBS. The cell pellet was resuspended in 1×PBS and the bacterial concentration was calibrated based on optical density. Dilutions were prepared in 1×PBS to obtain the required numbers of bacteria for infection. *Galleria* infections were performed as described previously (Mukherjee *et al.*, 2010). Briefly, the *L. monocytogenes* wild type strain

For Peer Review

EGD-e and the Δ*gpsB* mutant strain LMJR19 were injected separately (10^6 CFU/larva) into the hemocoel of the last instar larvae and the infection was monitored at 37°C for seven days.

Acknowledgements

We are grateful to Birgitt Hahn, Petra Kaiser and Gudrun Holland for technical assistance. We thank the beamline staff at the Diamond synchrotron for help and access to their facilities, Dr. Arnaud Baslé for help with X-ray data collection and analysis, and Dr. Tom Jowitt (University of Manchester's Biomolecular Analysis Core Facility) and Dr. Owen Davies of Newcastle University for SEC-MALLS. Electrospray ionization mass spectra were recorded at the Astbury Centre for Structural Molecular Biology and in the Department of Chemistry (CCIAS) at the University of Sheffield. This work has been supported by the DFG (HA 6830/1-1, to SH) and the UK BBSRC (BB/G015902/1 and BB/M001180/1, to RJL).

For Peer Review

References

Adams, D.W. & J. Errington, (2009) Bacterial cell division: assembly, maintenance and disassembly of the Z ring. *Nat Rev Microbiol* **7**: 642-653.

Adams, P.D., P.V. Afonine, G. Bunkoczi, V.B. Chen, I.W. Davis, N. Echols, J.J. Headd, L.W. Hung, G.J. Kapral, R.W. Grosse-Kunstleve, A.J. McCoy, N.W. Moriarty, R. Oeffner, R.J. Read, D.C. Richardson, J.S. Richardson, T.C. Terwilliger & P.H. Zwart, (2010) PHENIX: a comprehensive Python-based system for macromolecular structure solution. *Acta crystallographica. Section D, Biological crystallography* **66**: 213-221.

Bertsche, U., E. Breukink, T. Kast & W. Vollmer, (2005) *In vitro* murein peptidoglycan synthesis by dimers of the bifunctional transglycosylase-transpeptidase PBP1B from *Escherichia coli*. *J Biol Chem* **280**: 38096-38101.

Chen, V.B., W.B. Arendall, 3rd, J.J. Headd, D.A. Keedy, R.M. Immormino, G.J. Kapral, L.W. Murray, J.S. Richardson & D.C. Richardson, (2010) MolProbity: all-atom structure validation for macromolecular crystallography. *Acta crystallographica. Section D, Biological crystallography* **66**: 12-21.

Claessen, D., R. Emmins, L.W. Hamoen, R.A. Daniel, J. Errington & D.H. Edwards, (2008) Control of the cell elongation-division cycle by shuttling of PBP1 protein in *Bacillus subtilis*. *Mol Microbiol* **68**: 1029-1046.

Cowtan, K., (2006) The Buccaneer software for automated model building. 1. Tracing protein chains. *Acta crystallographica. Section D, Biological crystallography* **62**: 1002-1011.

Donovan, C., B. Sieger, R. Krämer & M. Bramkamp, (2012) A synthetic *Escherichia coli* system identifies a conserved origin tethering factor in *Actinobacteria*. *Mol Microbiol* **84**: 105-116.

Duman, R., S. Ishikawa, I. Celik, H. Strahl, N. Ogasawara, P. Troc, J. Lowe & L.W. Hamoen, (2013) Structural and genetic analyses reveal the protein SepF as a new membrane anchor for the Z ring. *Proc Natl Acad Sci U S A* **110**: E4601-4610.

Emsley, P., B. Lohkamp, W.G. Scott & K. Cowtan, (2010) Features and development of Coot. *Acta crystallographica. Section D, Biological crystallography* **66**: 486-501.

Eswaramoorthy, P., M.L. Erb, J.A. Gregory, J. Silverman, K. Pogliano, J. Pogliano & K.S. Ramamurthi, (2011) Cellular architecture mediates DivIVA ultrastructure and regulates min activity in *Bacillus subtilis*. *mBio* **2**. pii: e00257-11. doi: 10.1128/mBio.00257-11

Evans, P., (2006) Scaling and assessment of data quality. *Acta crystallographica. Section D, Biological crystallography* **62**: 72-82.

Evans, P.R. & G.N. Murshudov, (2013) How good are my data and what is the resolution? *Acta crystallographica. Section D, Biological crystallography* **69**: 1204-1214.

Fadda, D., C. Pischedda, F. Caldara, M.B. Whalen, D. Anderluzzi, E. Domenici & O. Massidda, (2003) Characterization of *divIVA* and other genes located in the chromosomal region downstream of the *dcw* cluster in *Streptococcus pneumoniae*. *J Bacteriol* **185**: 6209-6214.

Fleurie, A., S. Manuse, C. Zhao, N. Campo, C. Cluzel, J.P. Lavergne, C. Freton, C. Combet, S. Guiral, B. Soufi, B. Macek, E. Kuru, M.S. VanNieuwenhze, Y.V. Brun, A.M. Di Guilmi, J.P. Claverys, A. Galinier & C. Grangeasse, (2014) Interplay of the serine/threonine-kinase StkP and the paralogs DivIVA and GpsB in pneumococcal cell elongation and division. *PLoS genetics* **10**: e1004275.

Gamba, P., J.W. Veening, N.J. Saunders, L.W. Hamoen & R.A. Daniel, (2009) Two-step assembly dynamics of the *Bacillus subtilis* divisome. *J Bacteriol* **191**: 4186-4194.

Gola, S., T. Munder, S. Casonato, R. Manganelli & M. Vicente, (2015) The essential role of SepF in mycobacterial division. *Mol Microbiol* **97**: 560-576.

For Peer Review

Grayo, S., O. Join-Lambert, M.C. Desroches & A. Le Monnier, (2008) Comparison of the *in vitro* efficacies of moxifloxacin and amoxicillin against *Listeria monocytogenes*. *Antimicrob Agents Chemother* **52**: 1697-1702.

Halbedel, S., B. Hahn, R.A. Daniel & A. Flieger, (2012) DivIVA affects secretion of virulence-related autolysins in *Listeria monocytogenes*. *Molecular Microbiology* **83**: 821-839.

Halbedel, S., S. Reiss, B. Hahn, D. Albrecht, G.K. Mannala, T. Chakraborty, T. Hain, S. Engelmann & A. Flieger, (2014) A systematic proteomic analysis of *Listeria monocytogenes* house-keeping protein secretion systems. *Molecular & cellular proteomics : MCP* **13**: 3063-3081.

Hale, C.A. & P.A. de Boer, (1997) Direct binding of FtsZ to ZipA, an essential component of the septal ring structure that mediates cell division in *E. coli*. *Cell* **88**: 175-185.

Harbury, P.B., P.S. Kim & T. Alber, (1994) Crystal structure of an isoleucine-zipper trimer. *Nature* **371**: 80-83.

Hof, H., (2004) An update on the medical management of listeriosis. *Expert opinion on pharmacotherapy* **5**: 1727-1735.

Jakimowicz, D. & G.P. van Wezel, (2012) Cell division and DNA segregation in *Streptomyces*: how to build a septum in the middle of nowhere? *Mol Microbiol* **85**: 393-404.

Johansson, J., P. Mandin, A. Renzoni, C. Chiaruttini, M. Springer & P. Cossart, (2002) An RNA thermosensor controls expression of virulence genes in *Listeria monocytogenes*. *Cell* **110**: 551-561.

Kabsch, W., (2010) Xds. *Acta crystallographica. Section D, Biological crystallography* **66**: 125-132.

Kammerer, R.A., D. Kostrewa, P. Progias, S. Honnappa, D. Avila, A. Lustig, F.K. Winkler, J. Pieters & M.O. Steinmetz, (2005) A conserved trimerization motif controls the topology of short coiled coils. *Proc Natl Acad Sci U S A* **102**: 13891-13896.

Karimova, G., J. Pidoux, A. Ullmann & D. Ladant, (1998) A bacterial two-hybrid system based on a reconstituted signal transduction pathway. *Proc Natl Acad Sci U S A* **95**: 5752-5756.

Kaval, K.G. & S. Halbedel, (2012) Architecturally the same, but playing a different game: the diverse species-specific roles of DivIVA proteins. *Virulence* **3**: 406-407.

Krissinel, E. & K. Henrick, (2007) Inference of macromolecular assemblies from crystalline state. *J Mol Biol* **372**: 774-797.

Land, A.D., H.C. Tsui, O. Kocaoglu, S.A. Vella, S.L. Shaw, S.K. Keen, L.T. Sham, E.E. Carlson & M.E. Winkler, (2013) Requirement of essential Pbp2x and GpsB for septal ring closure in *Streptococcus pneumoniae* D39. *Mol Microbiol* **90**: 939-955.

Langer, G., S.X. Cohen, V.S. Lamzin & A. Perrakis, (2008) Automated macromolecular model building for X-ray crystallography using ARP/wARP version 7. *Nature protocols* **3**: 1171-1179.

Lemaire, S., F. Van Bambeke, M.P. Mingeot-Leclercq & P.M. Tulkens, (2005) Activity of three β-lactams (ertapenem, meropenem and ampicillin) against intraphagocytic *Listeria monocytogenes* and *Staphylococcus aureus*. *The Journal of antimicrobial chemotherapy* **55**: 897-904.

Lenarcic, R., S. Halbedel, L. Visser, M. Shaw, L.J. Wu, J. Errington, D. Marenduzzo & L.W. Hamoen, (2009) Localisation of DivIVA by targeting to negatively curved membranes. *EMBO J* **28**: 2272-2282.

Letek, M., E. Ordonez, J. Vaquera, W. Margolin, K. Flärdh, L.M. Mateos & J.A. Gil, (2008) DivIVA is required for polar growth in the MreB-lacking rod-shaped actinomycete *Corynebacterium glutamicum*. *J Bacteriol* **190**: 3283-3292.

For Peer Review

Lin, L. & M. Thanbichler, (2013) Nucleotide-independent cytoskeletal scaffolds in bacteria. *Cytoskeleton* **70**: 409-423.
Marquis, H., (2006) Tissue culture cell assays used to analyze *Listeria monocytogenes*. *Current protocols in microbiology* **Chapter 9**: Unit 9B 4.
Marston, A.L., H.B. Thomaides, D.H. Edwards, M.E. Sharpe & J. Errington, (1998) Polar localization of the MinD protein of *Bacillus subtilis* and its role in selection of the mid-cell division site. *Genes Dev* **12**: 3419-3430.
Massidda, O., D. Anderluzzi, L. Friedli & G. Feger, (1998) Unconventional organization of the division and cell wall gene cluster of *Streptococcus pneumoniae*. *Microbiology* **144 (Pt 11)**: 3069-3078.
McCoy, A.J., R.W. Grosse-Kunstleve, P.D. Adams, M.D. Winn, L.C. Storoni & R.J. Read, (2007) Phaser crystallographic software. *Journal of applied crystallography* **40**: 658-674.
Monk, I.R., C.G. Gahan & C. Hill, (2008) Tools for functional postgenomic analysis of *Listeria monocytogenes*. *Appl Environ Microbiol* **74**: 3921-3934.
Mukherjee, K., B. Altincicek, T. Hain, E. Domann, A. Vilcinskas & T. Chakraborty, (2010) *Galleria mellonella* as a model system for studying *Listeria pathogenesis*. *Appl Environ Microbiol* **76**: 310-317.
Nguyen, L., N. Scherr, J. Gatfield, A. Walburger, J. Pieters & C.J. Thompson, (2007) Antigen 84, an effector of pleiomorphism in *Mycobacterium smegmatis*. *J Bacteriol* **189**: 7896-7910.
Nguyen, L.T., J.C. Gumbart, M. Beeby & G.J. Jensen, (2015) Coarse-grained simulations of bacterial cell wall growth reveal that local coordination alone can be sufficient to maintain rod shape. *Proc Natl Acad Sci U S A* **112**: E3689-3698.
Oliva, M.A., S. Halbedel, S.M. Freund, P. Dutow, T.A. Leonard, D.B. Veprintsev, L.W. Hamoen & J. Löwe, (2010) Features critical for membrane binding revealed by DivIVA crystal structure. *EMBO J* **29**: 1988-2001.
Pichoff, S. & J. Lutkenhaus, (2005) Tethering the Z ring to the membrane through a conserved membrane targeting sequence in FtsA. *Mol Microbiol* **55**: 1722-1734.
Ramamurthi, K.S. & R. Losick, (2009) Negative membrane curvature as a cue for subcellular localization of a bacterial protein. *Proc Natl Acad Sci U S A* **106**: 13541-13545.
Ramirez-Arcos, S., M. Liao, S. Marthaler, M. Rigden & J.A. Dillon, (2005) *Enterococcus faecalis divIVA*: an essential gene involved in cell division, cell growth and chromosome segregation. *Microbiology* **151**: 1381-1393.
Rismondo, J., L. Möller, C. Aldridge, J. Gray, W. Vollmer & S. Halbedel, (2015) Discrete and overlapping functions of peptidoglycan synthases in growth, cell division and virulence of *Listeria monocytogenes*. *Mol Microbiol* **95**: 332-351.
Sambrook, J., E.F. Fritsch & T. Maniatis, (1989) *Molecular cloning : a laboratory manual,* p. 3 v. Cold Spring Harbor Laboratory Press, Cold Spring Harbor, N.Y.
Sammito, M., C. Millan, D.D. Rodriguez, I.M. de Ilarduya, K. Meindl, I. De Marino, G. Petrillo, R.M. Buey, J.M. de Pereda, K. Zeth, G.M. Sheldrick & I. Uson, (2013) Exploiting tertiary structure through local folds for crystallographic phasing. *Nature methods* **10**: 1099-1101.
Stein, N., (2008) CHAINSAW: a program for mutating pdb files used as templates in molecular replacement. *Journal of applied crystallography* **41**: 641-643.
Swaminathan, B. & P. Gerner-Smidt, (2007) The epidemiology of human listeriosis. *Microbes Infect* **9**: 1236-1243.
Tavares, J.R., R.F. de Souza, G.L. Meira & F.J. Gueiros-Filho, (2008) Cytological characterization of YpsB, a novel component of the *Bacillus subtilis* divisome. *J Bacteriol* **190**: 7096-7107.

For Peer Review

Testa, O.D., E. Moutevelis & D.N. Woolfson, (2009) CC+: a relational database of coiled-coil structures. *Nucleic Acids Res* **37**: D315-322.

van Baarle, S., I.N. Celik, K.G. Kaval, M. Bramkamp, L.W. Hamoen & S. Halbedel, (2013) Protein-protein interaction domains of *Bacillus subtilis* DivIVA. *J Bacteriol* **195**: 1012-1021.

Zheng, L., U. Baumann & J.L. Reymond, (2004) An efficient one-step site-directed and site-saturation mutagenesis protocol. *Nucleic Acids Res* **32**: e115.

For Peer Review

Figure legends

Figure 1: Features of *L. monocytogenes* GpsB.

(A) Multiple sequence alignment of selected GpsB proteins. Sequence identity is indicated by black boxes, similarity by grey-shading. Numbering is according to *L. monocytogenes* (*Lmo*) GpsB. The observed secondary structure is shown above the alignment. Abbreviations: *Bsu* – *Bacillus subtilis*, *Sau* – *Staphylococcus aureus*, *Sep* – *Staphylococcus epidermidis*, *Oih* – *Oceanobacillus ihyensis*, *Lin* – *Listeria innocua*, *Lwe* – *Listeria welshimeri*, *Bli* – *Bacillus licheniformis*, *Ban* – *Bacillus anthracis*, *Bth* – *Bacillus thuringiensis*, *Bce* – *Bacillus cereus*, *Bha* – *Bacillus halodurans*, *Gkl* – *Geobacillus kaustophilus*, *Lca* – *Lactobacillus casei*, *Efa* – *Enterococcus faecalis*, *Lpl* – *Lactobacillus plantarum*, *Spn* – *Streptococcus pneumoniae*, *Sth* – *Streptococcus thermophilus*, *Spy* – *Streptococcus pyogenes*, *Smu* – *Streptococcus mutans*. (B) Bacterial two-hybrid experiment analyzing the self-interaction of full-length *Lm*GpsB. The empty pUT18 and pU18C plasmid were included for control. (C) Bacterial two-hybrid experiment to analyze the effect of truncations and the V32A mutation on *Lm*GpsB self-interaction. (D-F) Dual axis plots of the SEC-MALLS analysis of *Bs*GpsB (D), *Bs*GpsB$_{1-68}$ (E) and *Bs*GpsB$_{69-98}$ (F); for clarity only the plots for the *Bs*GpsB proteins are shown, but the *Lm*GpsB proteins behaved similarly. Light scattering of the eluate from the gel filtration column (S200 *Bs*GpsB, S75 *Bs*GpsB$_{1-68}$, S200 *Bs*GpsB$_{69-98}$) is plotted as a function of elution volume (x-axis). Light scattering is plotted on the left hand y-axis and molecular masses (right hand y-axis) were calculated by extrapolation from Zimm plots; the monomer molecular weights of each construct are given in parentheses above the SEC-MALLS chromatogram.

For Peer Review

Figure 2: Subcellular localization of *L. monocytogenes* GpsB.

(A) Micrograph showing the fluorescence pattern of GpsB-GFP expressed in *L. monocytogenes* (strain LMS52). LMS52 cells were cultivated in BHI broth at 37 °C to mid-log growth phase and fluorescence images were taken (middle panel). Phase contrast (left) and merged images (right) are included. (B) Frequency plot to illustrate cell length frequency distributions of LMS52 cells with septal or non-septal fluorescence patterns of GpsB-GFP (236 cells measured in total). (C) Western blot to demonstrate full-length expression of GpsB-GFP. Cells of LMS10 (expressing GFP) and LMS52 were included as control and GFP proteins were visualized using an anti-GFP specific antiserum. (D) Western blots of cellular sub-fractions to demonstrate presence of GpsB in membrane fractions. Cells of strain EGD-e were grown in BHI broth at 37 °C to an optical density of OD_{600}=1.0, membrane and soluble protein fractions were isolated and tested in Western blots using antisera recognizing GpsB (upper panel) or DivIVA (middle panel). Strain LMS10 constitutively expressing GFP as a soluble cytosolic marker protein was included as control. (E) Effect of the L24A and R25A mutations on GpsB membrane association. GpsB levels in cellular and membrane fractions of strains EGD-e (wt), LMJR19 (Δ*gpsB*), LMJR68 (+L24A), and LMJR4 (+R25A) were analysed by Western blotting using a GpsB antiserum.

Figure 3: Growth of *L. monocytogenes* strains lacking *gpsB*.

(A) Growth of the Δ*gpsB* mutant LMJR19 in BHI broth at 30 °C. (B) Delayed growth of *L. monocytogenes gpsB* mutants in BHI broth at 37 °C. Strains EGD-e (wt), LMJR19 (Δ*gpsB*) and LMS56 (I*gpsB*, I – denotes IPTG-dependent expression) were grown in BHI broth (± 1 mM IPTG) at 37 °C and OD_{600} was measured. Insert: Lack of GpsB synthesis in *gpsB* mutant strains. Total cellular protein extracts were analyzed by Western blotting using a polyclonal anti-GpsB antiserum and purified, recombinant *Lm*GpsB-Strep was used as a control. Due to the Strep-Tag its molecular weight is slightly increased (14.1 kDa) in comparison to the

For Peer Review

untagged GpsB protein (12.9 kDa). (C) Growth defect *L. monocytogenes gpsB* mutants in BHI broth (± 1 mM IPTG) at 42 °C. Average values and standard deviations in all three experiments are calculated from three independent repetitions (but are too small to be seen in many cases).

Figure 4: The *L. monocytogenes* Δ*gpsB* mutant is prone to lysis.

(A) Phase contrast images of *L. monocytogenes* EGD-e (wt) and strain LMJR19 (Δ*gpsB*). Samples were taken from mid-log cultures, which had been grown in BHI broth at 37 °C. Scale bar is 5 µm. Arrows point to lysed phase bright cells. (B) Scanning electron micrographs showing cell morphology of the same set of strains cultivated under the same conditions at a 20,000-fold magnification. Scale bar is 2 µm. Images at a higher magnification are given in Fig. S3. (C) Penicillin susceptibility of *L. monocytogenes gpsB* mutant strains. *L. monocytogenes* strains EGD-e (wt), LMJR19, (Δ*gpsB*) and LMS56 (I*gpsB*) were used to inoculate BHI plates (containing 1 mM IPTG where indicated) and penicillin G high MIC test strips (0.016 - 256 µg mL^{-1}, Bestbiondx, Germany) were laid on top of the agar surface afterwards. Zones of growth inhibition became visible after one night of incubation at 37 °C. Minimum inhibitory concentrations (in µg mL^{-1}) are given at the bottom of each panel (D-E) Autolysis assay of *L. monocytogenes gpsB* mutant strains. The same set of strains as in panel C was grown in BHI broth (± 1 mM IPTG) at 37 °C to mid-log growth phase (OD_{600}~0.8). Cells were washed and resuspended in 50 mM Tris.HCl pH 8.0 and penicillin (D) or mutanolysin (E) was added at concentrations of 25 µg mL^{-1} and 10 U mL^{-1}, respectively. Decrease of optical density (λ=600 nm) is expressed as relative values. Average values and standard deviations are calculated from experiments performed in triplicate.

For Peer Review

Figure 5: Phenotype of a *L. monocytogenes* Δ*gpsB* Δ*divIVA* double mutant.

(A) Fluorescence micrographs showing Nile red stained cells of *L. monocytogenes* strains EGD-e (wt), LMJR19 (Δ*gpsB*), LMS2 (Δ*divIVA*), and LMJR28 (Δ*gpsB* Δ*divIVA*). Cells were taken from cultures that were grown in BHI broth at 37 °C until mid-logarithmic growth phase. Scale bar is 5 µm. (B) Frequency plot illustrating the distribution of cell lengths of the same set of strains under identical conditions. Approximately 300 cells were measured per strain.

Figure 6: *L. monocytogenes* GpsB controls function of PBP A1.

(A) Overexpression of all HMW PBPs in the *L. monocytogenes* Δ*gpsB* background. Strains EGD-e (wt), LMJR19 (Δ*gpsB*), LMJR31 (Δ*gpsB*+*pbpB3*), LMJR32 (Δ*gpsB*+*pbpB1*), LMJR33 (Δ*gpsB*+*pbpA1*), LMJR34 (Δ*gpsB*+*pbpB2*), and LMJR35 (Δ*gpsB*+*pbpA2*) were streaked on BHI agar plates containing 1 mM IPTG and grown over night at 37 °C. (B) Effect of PBP A1 overexpression on growth of the Δ*gpsB* mutant in liquid culture. Strains EGD-e (wt), LMJR19 (Δ*gpsB*), LMJR33 (Δ*gpsB*+*pbpA1*), and LMJR39 (wt+*pbpA1*) were grown in BHI broth ± 1 mM IPTG at 37 °C. For better visibility of the effect, growth curves are presented on a linear axis. (C) SDS PAGE showing IPTG-dependent overexpression of PBP A1 in strains LMJR39 (wt+*pbpA1*) and LMJR33 (Δ*gpsB*+*pbpA1*). Strains were grown under the same conditions and membrane fractions were isolated. PBPs were stained with bocillin-fl and samples were separated by SDS-PAGE (using 8 % polyacrylamide gels). (D) Effect of *pbpA1* deletion on growth of the Δ*gpsB* mutant at 42 °C. Strains EGD-e (wt), LMJR19 (Δ*gpsB*), LMS57 (Δ*pbpA1*), and LMJR38 (Δ*gpsB* Δ*pbpA1*) were grown in BHI broth at 42°C. (E) Suppression of the cell division defect of the Δ*divIVA* Δ*gpsB* double mutant by *pbpA1* deletion. Cell length distributions of strains EGD-e (wt), LMJR19 (Δ*gpsB*), LMJR28 (Δ*gpsB* Δ*divIVA*), and LMJR42 (Δ*gpsB* Δ*divIVA* Δ*pbpA1*) measured during exponential growth in BHI broth at 37 °C. Lengths of ~300 cells per strain were measured. (F) Synthetic lethality of

For Peer Review

gpsB with *pbpA2* as demonstrated by IPTG-dependence of the GpsB depletion strain LMJR108, which also lacks PBP A2. Strains EGD-e (wt), LMJR19 (Δ*gpsB*), LMS64 (Δ*pbpA2*) and LMJR108 (Δ*pbpA2* I*gpsB*) were cultivated in BHI broth ± 1 mM IPTG at 37 °C. Strain LMJR108 was pre-grown in an overnight culture containing IPTG, washed and used to inoculate a depletion culture not containing IPTG. After one day of growth, aliquots from such depletion cultures were used to start LMJR108 cultures ± IPTG as shown in this diagram. All growth curves show average values and standard deviations calculated from three independent repetitions.

Figure 7: GpsB interacts with PBP A1.

(A) Bacterial two hybrid assay showing the interaction of *Lm*GpsB variants with *Lm*PBP A1. Schematic illustrations of the GpsB variants used are given below. (B-E) Surface plasmon resonance of the *Bs*GpsB:*Bs*PBP1 interaction. (B) Binding of full length *Bs*GpsB fit according to a 1:1 interaction model, gives a K_d of 0.7±0.1 µM. Note a narrow protein concentration range is used for the fit because the fit to a 1:1 interaction model deteriorates on including binding data measured at higher protein concentrations, which may be due to multiple modes of binding of the multivalent *Bs*GpsB hexamer to immobilized *Bs*PBP1 molecules. (C) Raw sensorgrams for full-length *Bs*GpsB (black) and *Bs*$GpsB_{69-98}$ (red) injected over an SPR chip onto which full-length *Bs*PBP1 had been immobilized. Note that no binding of BSA (green dashes) was observed to the same *Bs*PBP1 SPR chip. (D) SPR analysis of the interaction of *Bs*$GpsB_{1-68}$ with a *Bs*PBP1-coated chip. The change in response units at various injected concentrations of $GpsB_{1-68}$ proteins are shown for both the wild type (solid line) and the D31A/D35A mutant (dashed line). Fitting these data to a 1:1 binding model gives a K_d of 30±4 µM for the wild type and 125±3 µM for the D31A/D35A mutant. (E) *Bs*GpsB did not bind demonstrably to SPR chips onto which *Bs*$PBP1_{32-914}$ had been immobilized. (F) Fluorescence polarization analysis of the interaction of *Bs*$GpsB_{1-68}$ (black)

For Peer Review

with the cytoplasmic domain (residues 1-32, C-terminally labelled with fluorescein) of *Bs*PBP1. Fitting the increase in fluorescence polarization to a 1:1 binding model gives a K_d of 90±10 µM for the interaction with wild type *Bs*GpsB$_{1-68}$. By contrast, the D31A/D35A mutant (red) does not increase the fluorescence polarization of the PBP1$_{1-32}$ peptide appreciably even at a concentration of 0.5 mM. Error bars correspond to the standard error from three measurements.

Figure 8: Structures of the GpsB N- and C-terminal domain.

(A) C_α trace of *Lm*GpsB$_{1-73}$ with each molecule in the dimer coloured independently; the positions of the residues that stabilise the four helix bundle of the dimer are highlighted in grey. Additional hydrophobic amino acids that are part of the coiled coil heptad motif are labelled in black. All panels show the same perspective of *Lm*GpsB$_{1-73}$. (B) C_α trace of superimposed structures of *Lm*GpsB$_{1-73}$ (cyan) and *Bs*GpsB$_{1-68}$ (red). (C) Ribbon diagram of a representative trimer of *Bs*GpsB$_{76-98}$; terminal amino acids are labelled. (D) Key interactions characteristic of parallel three stranded coiled coils are found in the *Bs*GpsB$_{76-98}$ trimer; the role of residues drawn in stick representation are described in the text. R83 and E88 in the *Bs*GpsB$_{76-98}$ correspond to R96 and E101 in *L. monocytogenes* GpsB (Fig. S1A). (E) Surface electrostatic potential of *Lm*GpsB$_{1-73}$, with negative charge coloured red and positive charge blue. (F) Surface representation of sequence conservation; the darkest purple shade maps to the most conserved residues in a GpsB alignment and the darkest shade of aquamarine maps to the least conserved. Yellow residues cannot be assigned a reliable conservation score as they only align with a few sequences in the overall alignment. (G) Alanine scanning mutagenesis of *Lm*GpsB to identify residues important for *Lm*PBP A1 binding by bacterial two-hybrid. (H) Surface representation of *Lm*GpsB$_{1-73}$ in salmon, where blue and green patches represent the residues important for PBP A1 binding (Y27, D33, D37, I40) or self-interaction (V32, L36), respectively.

For Peer Review

Figure 9: Mutational analysis of structurally relevant amino acids in *Lm*GpsB.

(A) Growth of strains LMJR68 (L24A), LMJR4 (R25A), LMJR130 (Y27A), LMJR131 (V32A), LMJR132 (L36A), LMJR133 (D37A), LMJR134 (I40A), and LMJR135 (D33A), in BHI broth containing 1 mM IPTG at 42 °C. All strains were Δ*gpsB* mutants ectopically expressing GpsB mutant proteins with amino acid exchanges in the N-terminal domain of GpsB at positions required for lipid binding (L24, R25), dimerization (V32, L36) or PBP A1 binding (Y27, D33, D37, I40). Strains EGD-e (wt), LMJR19 (Δ*gpsB*), LMS56 (Δ*gpsB*+*gpsB*) were included as controls. For better clarity, a representative growth curve is shown. (B) Western blots showing GpsB expression in the same set of strains during growth at 37 °C. Detection of DivIVA was performed as loading control. (C) Mapping of the same mutations onto the *Lm*GpsB$_{1-73}$ crystal structure. (D) Complementation assay comparing growth of strains EGD-e (wt), LMJR19 (Δ*gpsB*), LMS56 (Δ*gpsB*+*gpsB*), LMJR163 (R96A), and LMJR164 (E101A) in BHI broth containing 1 mM IPTG at 42 °C. Growth curves show average values and standard deviations calculated from three independent repetitions. (E) Western blot analyzing expression of GpsB proteins in the same set of strains during growth at 37°C; again, DivIVA was used as control. (F) Blue native PAGE of full-length *Lm*GpsB-Strep and R96A and E101A variants thereof. *Lm*GpsB$_{1-89}$-Strep lacking the C-terminal domain was included as negative control.

Figure 10. Role of GpsB in virulence

(A) *L. monocytogenes* strains EGD-e (wt) and the Δ*gpsB* mutant (LMJR19) were used to infect monolayers of J774.A1 mouse ascites macrophages. Sampling for monitoring of intracellular growth was performed in two-hour intervals. The experiment was performed in triplicate and standard deviations are shown (but too small to be seen in some cases). Significance levels (t-test) are indicated by asterisks (* P<0.05; ** P<0.005). (B) Plaque formation assay to analyse cell-to-cell spread. *L. monocytogenes* strains EGD-e (wt) and

For Peer Review

LMJR19 (Δ*gpsB*) were used to infect a confluent layer of 3T3 mouse embryo fibroblasts. Plaques indicate zones of host cell killing and are visualized three days post infection by counterstaining with neutral red. (C) Survival curves of *Galleria mellonella* larvae infected with *L. monocytogenes* strains EGD-e (wt) and LMJR19 (Δ*gpsB*). Mock infections using NaCl solution were included as negative control. Results represent average values of three independent experiments with a total of 10 larvae per treatment. Significance levels are labelled as described above.

For Peer Review

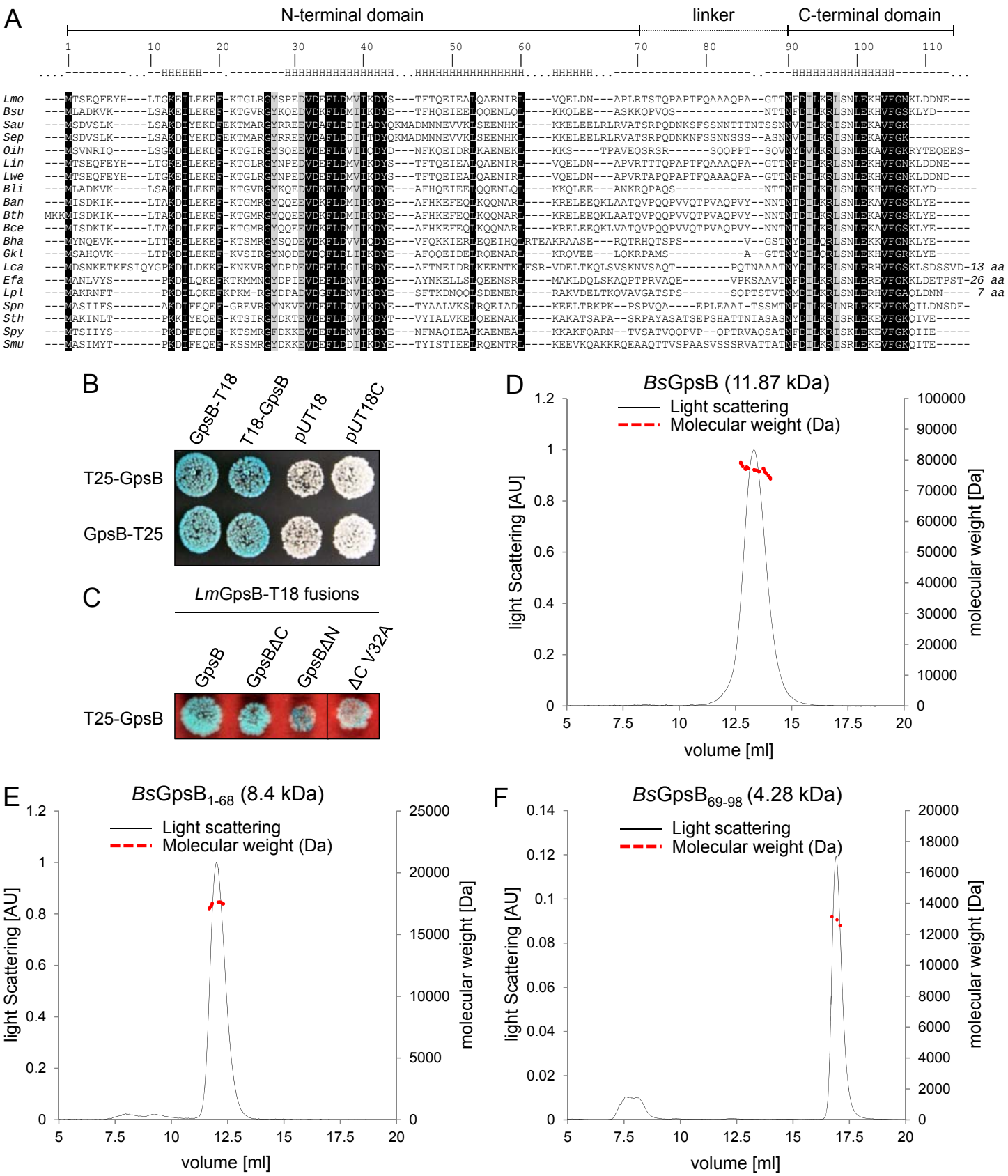

Rismondo *et al.*, Fig. 1

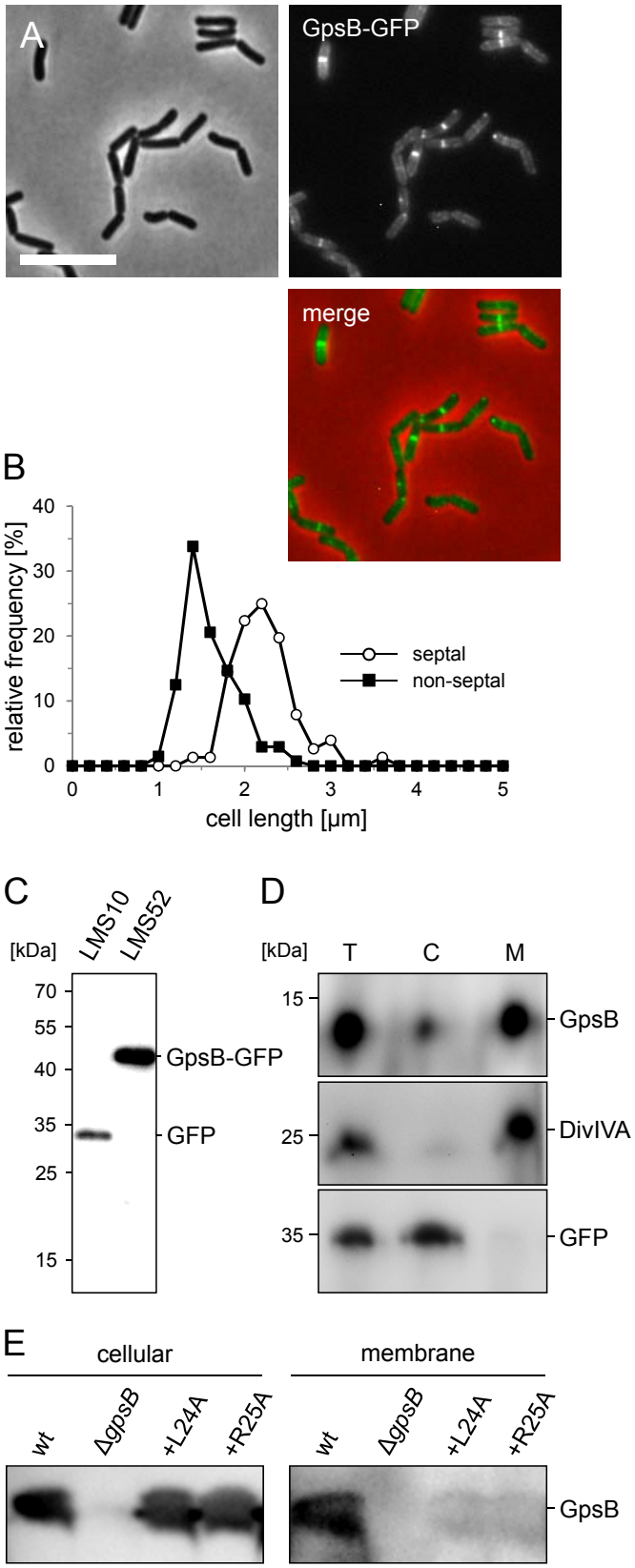

Rismondo *et al.*, Fig. 2

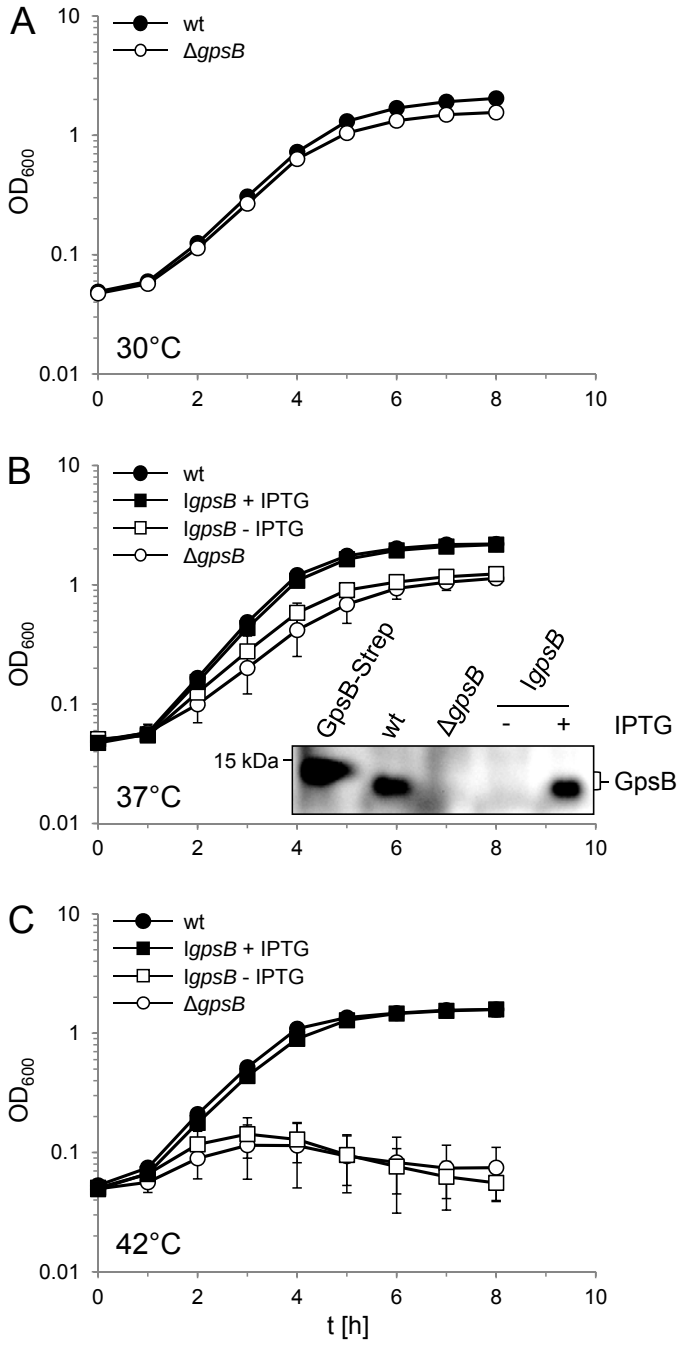

Rismondo *et al.*, Fig. 3

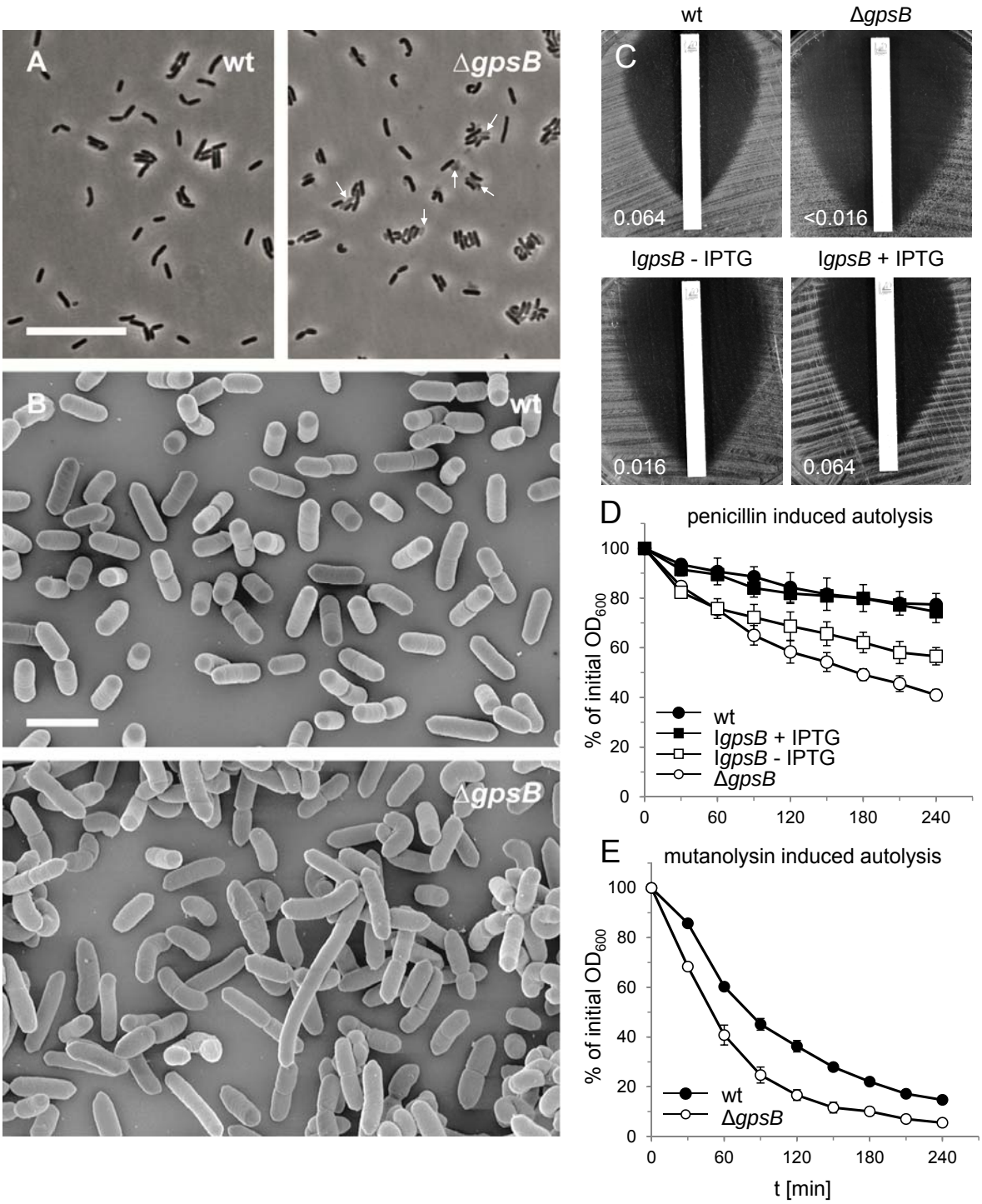

Rismondo *et al.*, Fig. 4

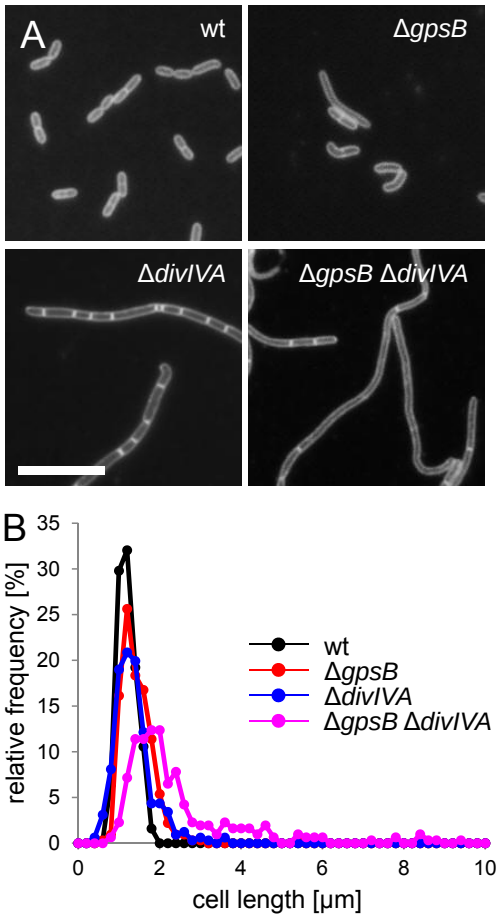

Rismondo *et al.*, Fig. 5

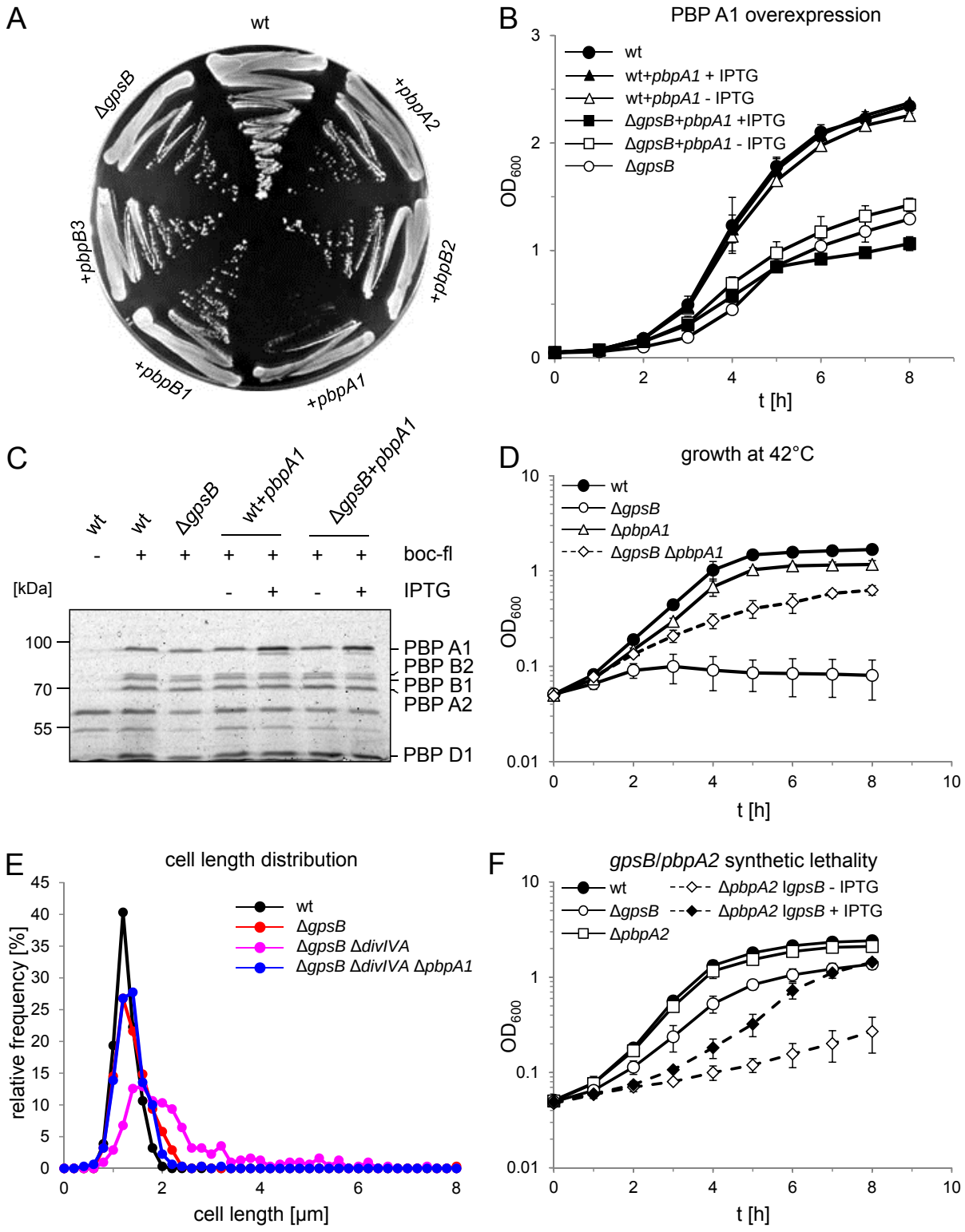

Rismondo *et al.*, Fig. 6

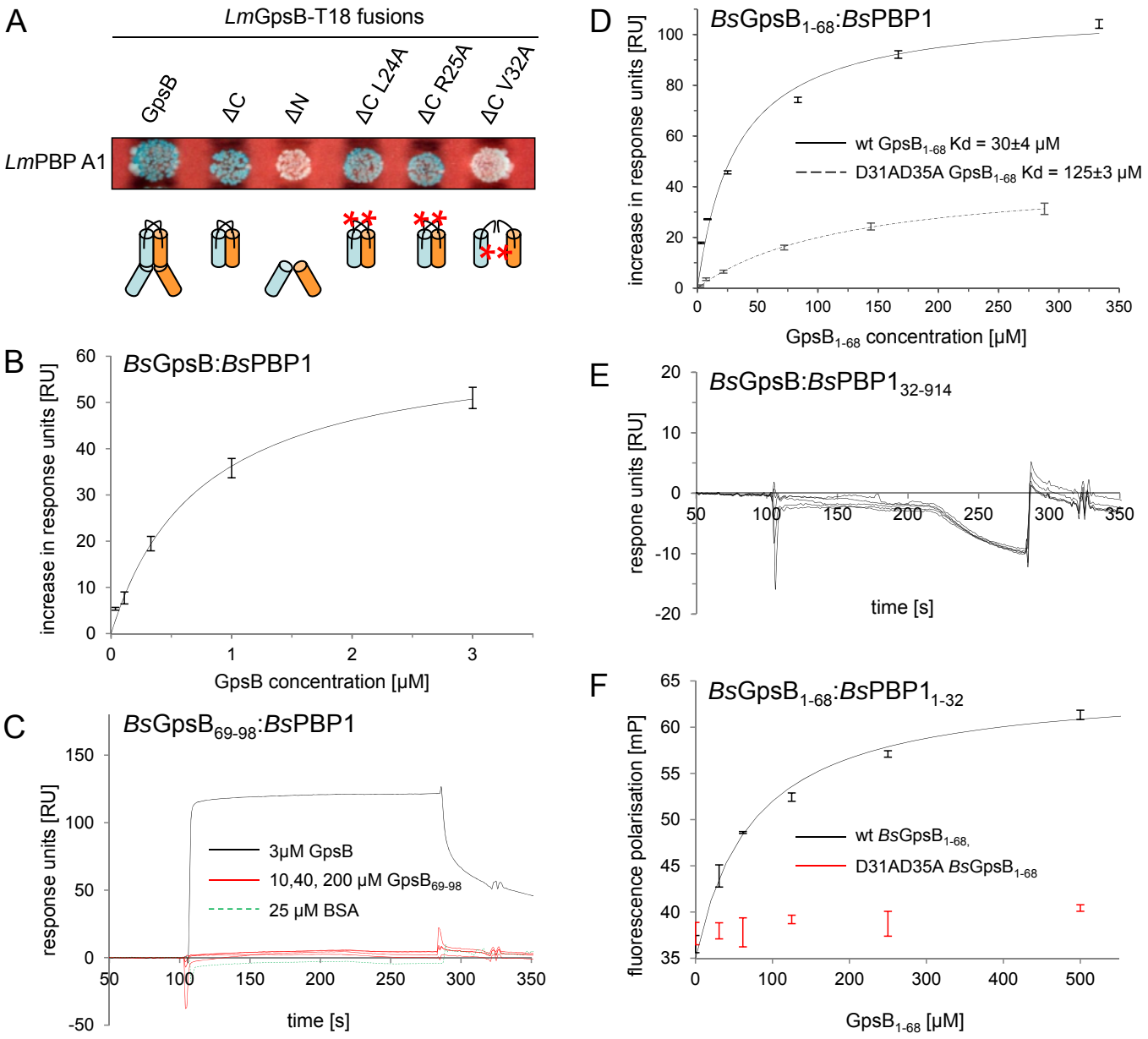

Rismondo *et al.*, Fig. 7

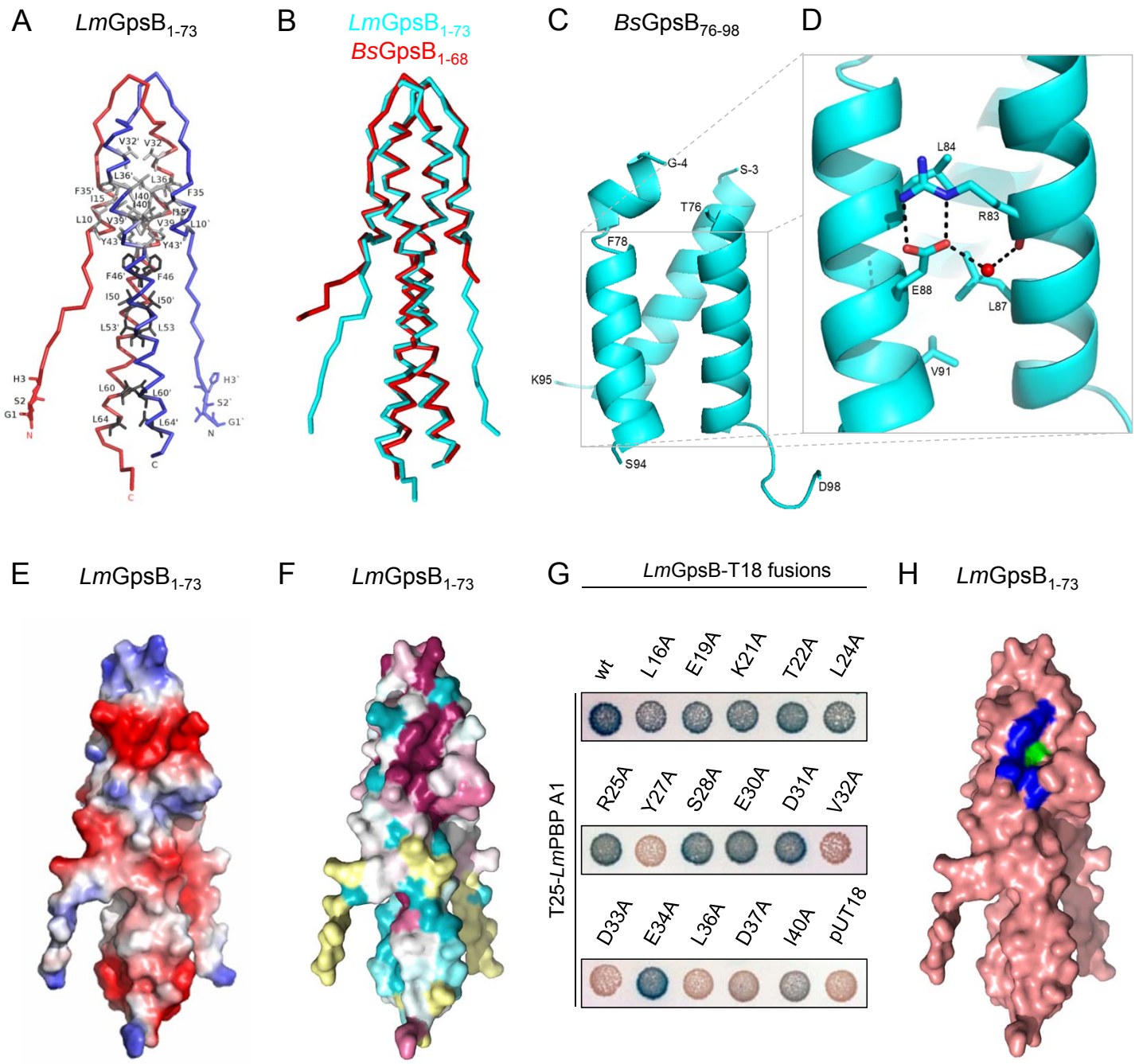

Rismondo *et al.*, Fig. 8

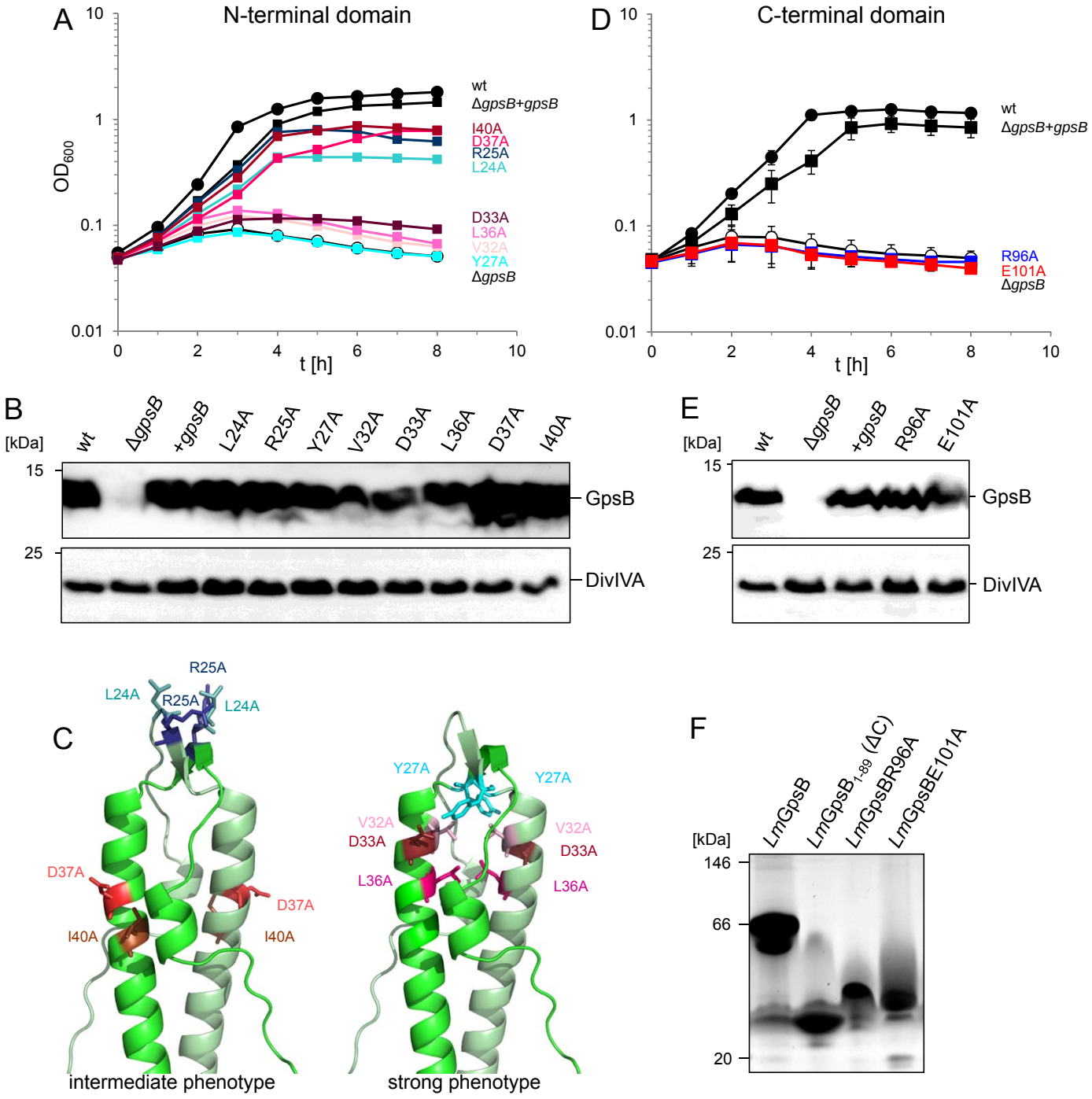

Rismondo *et al.*, Fig. 9

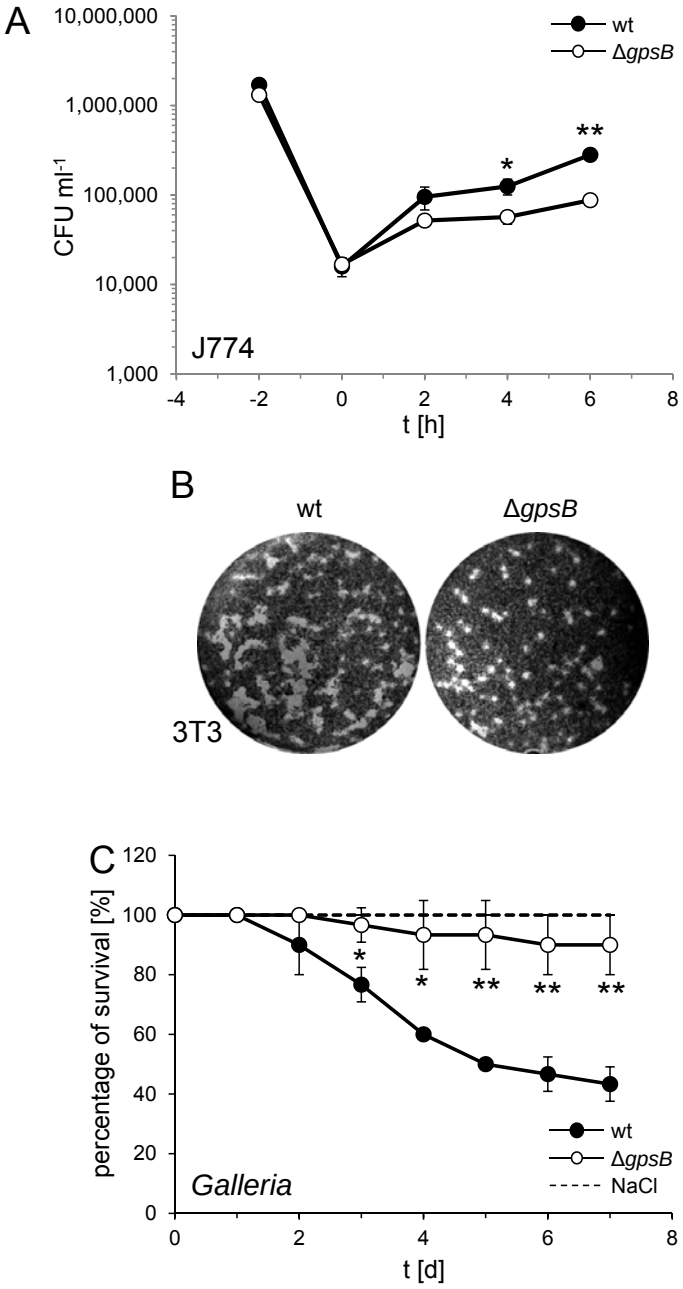

Rismondo *et al.*, Fig. 10

Abbreviated Summary

GpsB is a cell division protein and conserved in many Gram-positive bacteria. Here we describe its function in growth, cell division and cell wall biosynthesis of the important human pathogen *Listeria monocytogenes*. Analysis of the three-dimensional structure of GpsB now explains how GpsB binds to its interaction partner, the major bi-functional penicillin binding protein PBP A1.

For Peer Review

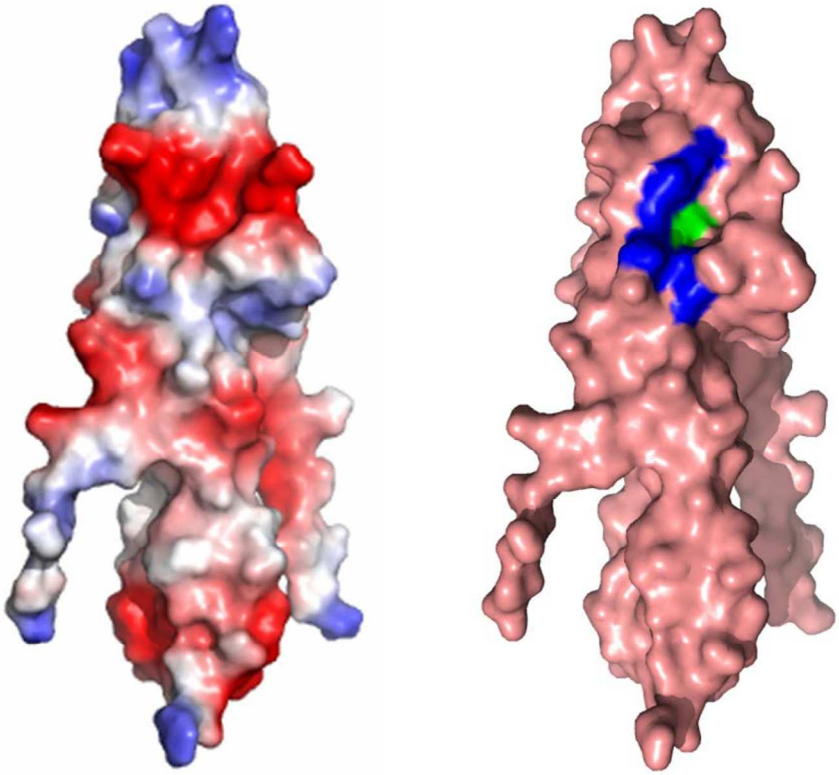

Structure of the N-terminal domain of L. monocytogenes GpsB.
(Left) Surface electrostatic potential of LmGpsB1-73, with negative charge coloured red and positive charge blue. (Right) Surface representation of LmGpsB1-73 in salmon, where blue and green patches represent the residues important for PBP A1 binding (Y27, D33, D37, I40) or self-interaction (V32, L36), respectively.

299x261mm (150 x 150 DPI)

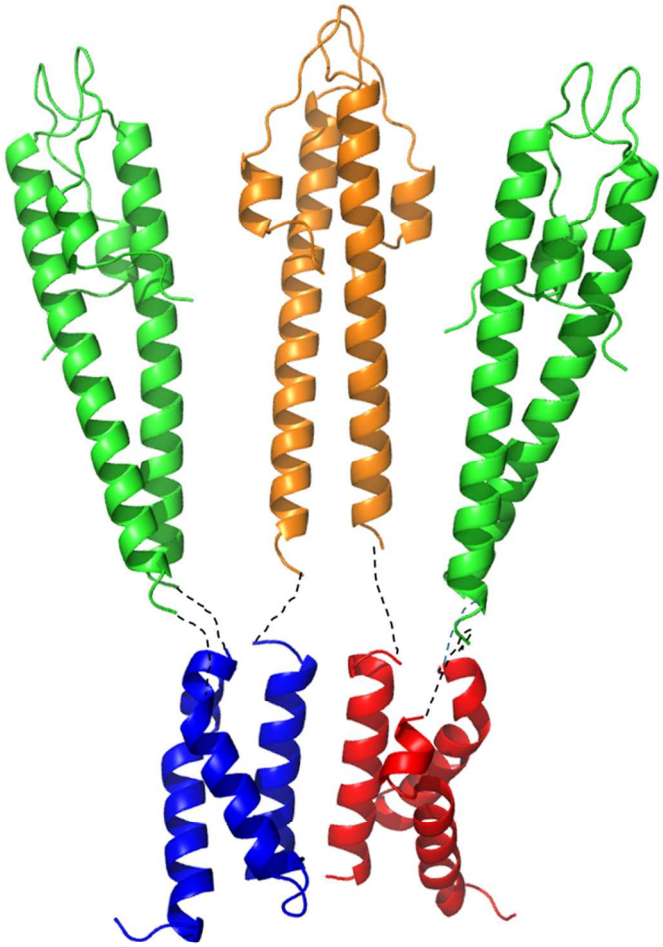

Model of the GpsB hexamer from Bacillus subtilis. Crystal structures of the N- and C-terminal domains were solved separately and combined as suggested by biochemical data.
156x216mm (149 x 149 DPI)